INFORMATION TO USERS

This manuscript has been reproduced from the microfilm master. UMI films the text directly from the original or copy submitted. Thus, some thesis and dissertation copies are in typewriter face, while others may be from any type of computer printer.

The quality of this reproduction is dependent upon the quality of the copy submitted. Broken or indistinct print, colored or poor quality illustrations and photographs, print bleedthrough, substandard margins, and improper alignment can adversely affect reproduction.

In the unlikely event that the author did not send UMI a complete manuscript and there are missing pages, these will be noted. Also, if unauthorized copyright material had to be removed, a note will indicate the deletion.

Oversize materials (e.g., maps, drawings, charts) are reproduced by sectioning the original, beginning at the upper left-hand corner and continuing from left to right in equal sections with small overlaps. Each original is also photographed in one exposure and is included in reduced form at the back of the book.

Photographs included in the original manuscript have been reproduced xerographically in this copy. Higher quality 6" x 9" black and white photographic prints are available for any photographs or illustrations appearing in this copy for an additional charge. Contact UMI directly to order.

U·M·I

University Microfilms International
A Bell & Howell Information Company
300 North Zeeb Road, Ann Arbor, MI 48106-1346 USA
313/761-4700 800/521-0600

A

PLANAR TO CELLULAR BIFURCATIONS DURING DIRECTIONAL SOLIDIFICATION

by

DONGNING LIU

A dissertation submitted to the Graduate Faculty in Physics in partial fulfillment of the requirements for the degree of Doctor of Philosophy, The City University of New York.

1995

UMI Number: 9530897

UMI
300 North Zeeb Road
Ann Arbor, MI 48103

This manuscript has been read and accepted for the Graduate Faculty in Physics in satisfaction of the dissertation requirement for the degree of Doctor of Philosophy.

4/24/95
Date

Chair of Examining Committee

4/27/95
Date

Joseph B. Krieger
Executive Officer

K. H. Becker
P.E. Cladis
H.Z. Cummins
J. Koplik
R.A. Marino
Supervisory Committee

The City University of New York

Abstract

PLANAR TO CELLULAR BIFURCATIONS
DURING DIRECTIONAL SOLIDIFICATION

by

Dongning Liu

Advisor: Professor Herman Z. Cummins

Equilibrium phase transitions with primary and secondary control parameters may exhibit a line of first order transitions which passes through a tricritical point and becomes a line of second-order transitions. The Mullins-Sekerka planar-cellular instability in directional solidification should be subcritical when the partition coefficient $k<0.45$ and supercritical when $k>0.45$ if latent heat is ignored. However, Merchant and Davis [Phys. Rev. Lett. 63, 573 (1989)] predicted that as the solute concentration is reduced, the increasingly important thermal diffusion field could lead to a crossover from a subcritical to a supercritical bifurcation, producing a dynamical analogue of the tricritical point. We have designed and assembled a precision directional solidification apparatus integrated with an externally controlled laser perturbation mechanism in order to test this prediction.

Directional solidification experiments were performed on a series of succinonitrile samples containing different concentrations of Coumarin 152. We have found evidence for the predicted crossover at a Coumarin concentration $C_t \sim 0.1$ wt%. In the subcritical regime, the velocity V_C^+ at which the initial planar interface first becomes unstable with increasing V and the velocity V_C^- at which the cellular pattern reverts to planar with decreasing V determine the velocity hysteresis region $\Delta V = (V_C^+ - V_C^-)$. We find that ΔV decreases with decreasing c, and $\Delta V \sim 0$ for $c \leq 0.1$ wt%. A laser pulse with controlled power and duration was applied to the metastable ($V_C^+ < V < V_C^-$) planar interface to provide a local heat perturbation. Depending on the pulling speed, i.e. V close to V_C^+ or V_C^-, and also on the magnitude of the perturbation, the metastable planar interface either responds stably and relaxes back to a planar interface at different rates, or else the perturbation grows and the planar interface eventually evolves into a cellular pattern.

To my parents,

for their faith in an education.

Acknowledgments

I would like to thank Professor Cummins for his patient guidance, advice and support throughout my dissertation research, and for making my graduate study a most worthwhile and enjoyable experience. Thanks also to all the members of my thesis committee, for their time, discussions and guidance towards the completion of my dissertation research. I've enjoyed the many hours I spend with all my colleagues in the lab, Dr. Bill Shi, Dr. Lloyd Williams, Dr. Gen Li, Wolfgang Losert, Tracy Turner, Weimin Du and Joel Hernandez. In particular I would like to thank Dr. Shi and Dr. Williams for their support and help. I cannot forget the always friendly support from Hongfeng Du of our electronics shop. My special gratitude also goes to Mr. Joseph Altmann, director of our machine shop and the two machinists -- Mr. Joseph Duke and Linden Langhorne. His expertise advice and their precise and creative machining have made my experimental apparatus possible, building up a successful foundation for my experiments. There are many friends who helped me in big or small ways during my study here, I'd like to thank them all. I thank my parents for teaching me to value education and knowledge and my sisters for their steady support. My lovely daughter, Connie, always gives me endless happiness and strength. I'm especially indebted to my wife Hua for her trust in me and the love she gave to me, even when I was at my most unbearable. I wish I could find words to fully express my thanks to her.

Table of Contents

List of Table

Lists of Figures

1. Introduction

1.1 Introduction

Pattern formation occurs in a surprising variety of fields and over a wide range of length scales: from the microstructures of solidifying alloys, laboratory-sized patterns in hydrodynamics experiments, biological shapes, snow flakes, to atmospheric phenomena such as lightning patterns and "cloud streets", and even up to the large-scale structure of the universe! They all share a common intrinsic phenomenology in that systems driven far from equilibrium that are initially smooth can become unstable against formation of spatial (and sometimes temporal) patterns. For scientists, such a fascinating diversity has always been an inexhaustible source of questions as well as clues to applied science and pure physics laws. The first attempt on record to formulate this topic mathematically goes back to J. Kepler [1](1611) who, in his celebrated book "On the Six-Cornered Snowflake", recognized that snowflakes could not possibly always have six arms by chance and predicted the underlying atomic order from simple observations of snowflake symmetry.

As usual, the strategy which allows one to tackle these problems and to extract their essence consists in looking for the simplest systems rich enough to demonstrate the behavior under study. The most obvious way of decreasing complexity lies in the reduction of dimensions. Thus directional solidification of thin samples, among many other pattern-forming instabilities at one-dimensional fronts, is of particular interest for scientific as well as technological reasons because it is a fundamental metallurgical and crystal growth technique [2]. Historically, simple cast objects (in copper) first appeared before about 4000BC and the production of the renowned and highly sophisticated bronze castings of China began in about 1600BC. When materials are prepared by solidification of a melt, the advancing solid-liquid interface can undergo a range of morphological instabilities leading to complex forms with cellular or dendritic structures (see Figure 1). These resulting microstructures which may look like a collection of overly ambitious snowflakes [3] can strongly influence the mechanical properties of solids [4, 5] (see Figure **2** as an example for the microscopic structure of a Cu-Zn alloy.). However, their study in metals is exceedingly difficult because the materials are opaque and their melting temperatures are very high.

A major experimental advance took place in 1966 when Jackson and Hunt[6] showed that these phenomena can also occur in transparent plastic crystals where the evolution of an instability can be observed in situ. Directional solidification in plastic crystals then became an essential probe to study solidification processes and nonlinear dynamics, opening the field to quantitative study of the dynamics of solidification and pattern forming instabilities.[7] [8]

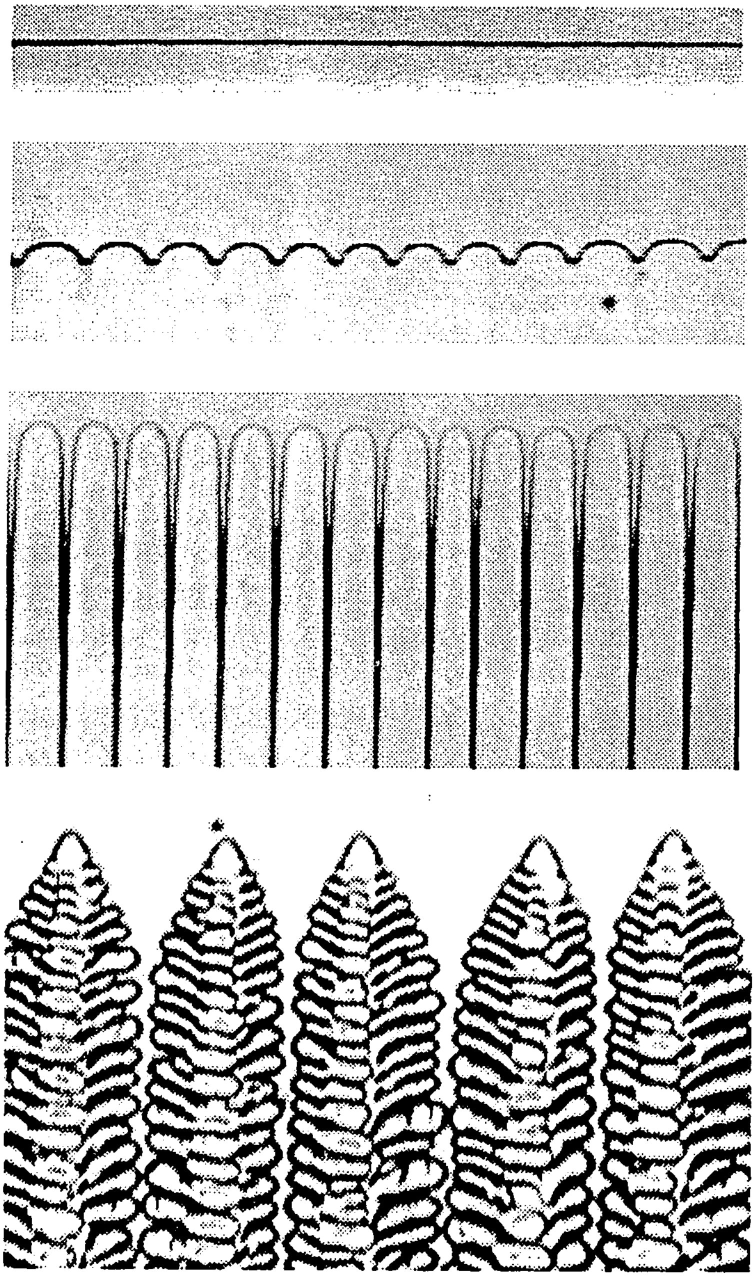

Figure 1 Pattern forming instabilities on the crystal-melt interface of a binary alloy of succinonitrille-coumarin during directional solidification. From top to bottom: planar interface, cellular interface, deep cells and dendritic arrays.

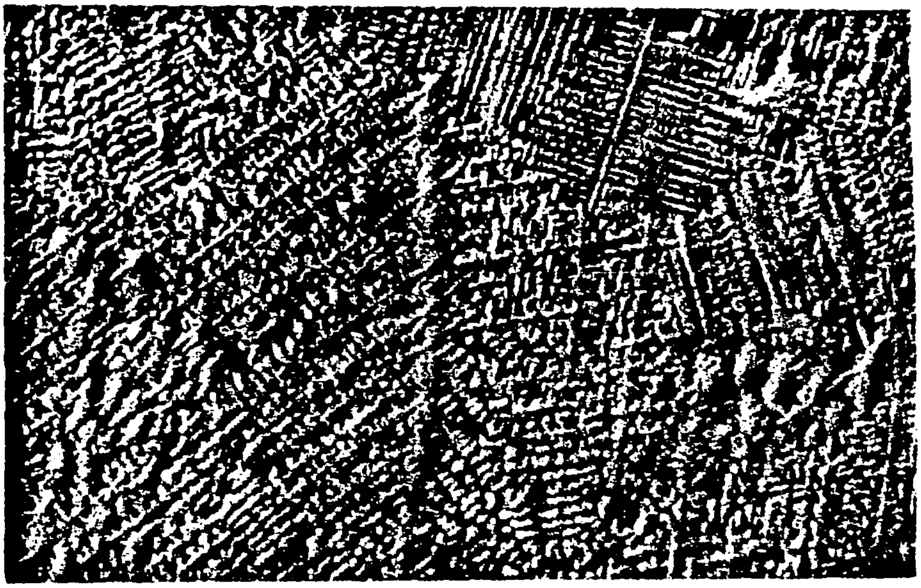

Figure 2 Micrograph of a cast Cu-Zn alloy (commercial 70/30 brass). In this sample, etched to show its microstructure, the dendrites solidified first, leaving impurity-rich liquid to solidify later in the interstices. The region swept out by each primary dendrite and its array of sidebranches is (very nearly) a single crystal, or grain, whose symmetry and orientation are the same as those of the dendrite. Thus the dendritic solidification mechanism determines both the grain structure and the patterns of chemical composition within the grain. (Reproduced from J.S. Langer, Physics Today, October 1992.)

Experimentally, one establish a temperature gradient in the plane of a (nearly) two dimensional sample (adding an impurity to induce pattern formation) such that the sample is solid at one end and liquid at the other. The sample is then moved at a constant velocity V along the direction of the gradient toward the cold end: As the liquid solidifies, the interface at steady-state freezes at -*V*, remaining at constant temperature. At low velocities, the interface remains a straight line; at high velocities, the interface destabilizes into a wavy pattern (see also Figure 1). This procedure is depicted schematically in Figure 3. (For more details about the experimental apparatus, see Chapter 3.)

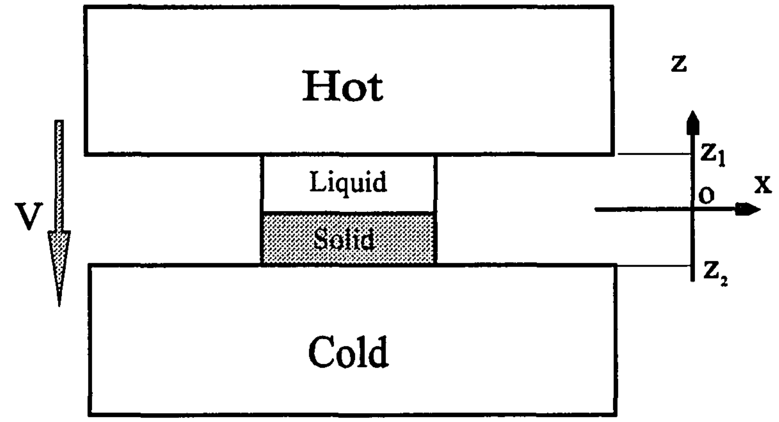

Figure 3 Schematic Illustration of a Directional Solidification Experiment.

In this thesis, we will be primarily interested in studying the physics of the planar to cellular transition.[9] After reviewing previous experimental work on subcritical and supercritical bifurcations, we then go through the theory in detail in Chapter 2. In Chapter 3, we discuss the design and construction of our directional solidification apparatus and the procedures followed in making the samples. The first experimental attempt to test the prediction of a subcritical to supercritical crossover during directional solidification is presented in Chapter 4. Subsequently we present a preliminary examination of the reaction of the metastable planar interface to a local heat perturbation generated by a laser pulse introduced via a laser-fiber coupling mechanism and investigate the two-phase dynamics of planar to cellular transitions. Finally we summarize our results in Chapter 5.

1.2 Overview of Previous Work

In 1964, Mullins and Sekerka [10] carried out a linear stability analysis for the two dimensional planar interface of a dilute binary alloy undergoing directional solidification. Their analysis showed that, for a given temperature gradient G and solute concentration c, there is a critical pulling speed V_C. For $V<V_C$ the planar interface is stable; for $V=V_C$ it becomes marginally stable against an infinitesimal fluctuation with a unique spatial wave number q_C; for $V>V_C$ there is a band of unstable wave numbers whose width initially increases rapidly with increasing V, and eventually decreases again as the interface approach restablization. (The possible existence of a wavelength selection mechanism within this band is an unresolved problem[11]). The subcritical or supercritical nature of the Mullins-Sekerka planar-cellular bifurcation cannot be identified from the linear analysis.

In 1982, Caroli, Caroli and Roulet [12], extending earlier work by Wollkind and Segel for the one-sided model [13], by Langer and Turski [14] and by Ungar and Brown [15] for the symmetric model, analyzed for the two-sided model the Landau equation of motion (i.e., an amplitude equation) for the amplitude ζ_q of a mode with wave number q:

$$\frac{d\zeta_q}{dt} = a_0\zeta_q - a_1\zeta_q^3 + \text{higher order terms} \qquad (1.1)$$

where a_0 , proportional to V, is the linear growth rate, and the sign of the Landau coefficient a_1 determines if the planar-cellular bifurcation is subcritical or supercritical (as discussed in detail in section 2.4.1). A general review of amplitude equation formulations of pattern formation was given by Hohenberg and Cross in 1987.[16] Caroli et al.[12] found that for V and G both small, in the high-concentration case where latent heat can be neglected and with the thermal conductivities assumed equal, $a_1 \propto (k^2 + 4k - 2)$, where k is the partition coefficient of the binary alloy. Hence, with latent heat neglected, the nature of the bifurcation only depends on the particular material via the value of k. For $k>0.45$, $a_l>0$ and the bifurcation is supercritical; for $k<0.45$, $a_l<0$ and the bifurcation is subcritical.

Several experiments were carried out to test this prediction. De Cheveigne, Guthmann and Lebrun [17,18] performed directional solidification experiments on CBr_4 with 1% Br_2 impurities (k was estimated as about 0.16) and found both hysteresis and discontinuous amplitude jumps characteristic of a subcritical bifurcation. Eshelman and Trivedi [19] studied succinonitrile with acetone impurity at concentrations between 0.10 and 0.34 wt%, and also concluded that in this system (for which k=0.10), the transition is subcritical. Bechhoefer and coworkers [20] studied a liquid crystal system with k~0.9 and found that the bifurcation is supercritical, again as predicted. A summary of theoretical values of a_l for a variety of materials was given by de Cheveigne et al.[21]. These measurements are very difficult, requiring long times to reach steady state.[22] The observations can also be complicated by three-dimensional effects, particularly in thick samples, as discussed by Cladis, Finn, and Gleeson [23], by de Cheveigne et al.[18].

Alexander et al. [24] extended the nonlinear analysis by including the latent heat in the condition describing the local balance of energy across the moving interface. Allowing for a finite latent heat results in a positive addition to the Landau coefficient a_l, and may therefore produce a supercritical bifurcation even though $k < 0.45$, especially at low solute concentrations. Merchant and Davis [25,26] have discussed this analysis without invoking the low-pulling speed approximation. They pointed out that by including the latent heat in the analysis, the critical velocity for SCN-acetone is shifted significantly compared to that for latent heat L=0, bringing regions of supercritical bifurcation into an experimentally accessible parameter range. They concluded that as the solute concentration is decreased and the critical velocity increases, the thermal diffusion effects becomes increasingly important. They found that a_l should change sign at a crossover point where the bifurcation should change from subcritical to supercritical. They found that this crossover point should be experimentally accessible for succinonitrile-acetone mixtures, and should occur close to the compositions studied by Eshelman and Trivedi [19].

Another approach to the study of this bifurcation was also discussed by Eshelman and Trivedi [19] who increased the growth velocity into the hysteresis region where the interface is predicted to be linearly stable, but nonlinearily unstable. After about three hours, a large fluctuation occurred spontaneously, and the evolution of the interface was then monitored.

In most of these experiments, the evolution of the wavelength of the cellular pattern was studied as the velocity was increased beyond the instability threshold.[27,28,29,] We note that the theoretical basis for wavelength selection (or even whether any selection mechanism exists) is still not known.[11,30,31,32] De Cheveigne et al. [33] summarized the threshold of the initial instability and the initial wavelength of the bifurcation from planar to cellular interface for both organic and metal alloys. In the low velocity limit, the linear analysis of directional solidification predicts a wavelength λ_C of the first marginally stable deformation of the interface[33]

$$\lambda_C = 2\pi\left(\frac{2T_M\sigma kD_L^2}{mL(k-1)}\right)^{1/3}\frac{1}{c_\infty^{1/3}}\frac{1}{V_C^{2/3}} \qquad (1.2)$$

where the physical parameters in the above equation are defined in section 2.1. Experimental results on the critical velocity have generally indicated a reasonable agreement with the linear stability analysis. In the experiments carried out by De Cheveigne et al [17], the critical velocity agrees with the one-dimensional calculation, if one chooses the sample (CBr_4-Br_2) with proper thickness and neglects the meniscus effect. In the study of succinonitrile-acetone by Eshelman and Trivedi [19], the critical velocity is found to be correct to within 20%. They were able to reduce this discrepancy by taking into account the change in solute concentration that takes place at the interface when the pulling speed is suddenly changed. However, at just above V_C, the initial wavelength of the unstable interface has been found to be significantly smaller than that predicted by the linear analysis. For example, de Cheveigne et al [17,18] found that the threshold value of the wavelength was smaller by a factor 2-3 than λ_C predicted by the linear theory (equation 1.2), Eshelman and Trivedi [19] observed a critical wavelength smaller by a factor of 3-4 than the predicted value. This discrepancy may be, in part, due to the shape of velocity-wavelength marginal stability curve (Figure 11) near V_C, which is very broad. This makes it difficult to determine experimentally the exact value of the wavelength at critical velocity since a slightly larger velocity will give a large range of unstable wavelengths. We note that for pulling speeds well above V_C, the initial wavelength of the cellular pattern is generally larger than that of the maximally unstable mode of the Mullins-Sekerka analysis. We also point out that the linear stability prediction of equation (1.2) is only useful for supercritical bifurcations since it supposes that the amplitude of the perturbation is infinitesimal. On the contrary, if the bifurcation is subcritical, there are no neighboring stable low-amplitude states that develop continuously from the planar state and the system undergoes a finite jump from planar to cellular states for which the linear prediction of λ_C does not apply.

Since the comprehensive review by Langer in 1980, there has been an extensive theoretical effort to understand how morphologic instability occurs,[34,35,36,37] and how the resulting steady-state patterns are selected.[38,39,40] It has been found that in general cellular or dendritic morphologies result from selective amplification of the infinitesimal perturbations due to microscopic noise at the interface [41, 42, 43, 44 45]. It is important to understand the dynamic processes of these pattern forming instabilities[46]. Gleeson and Cladis [47] studied the traveling-waves states (or the invasion of cells into the planar interface) by tilting the sample at a small angle to break the symmetry. Eshelman and Trivedi [19] have driven the succinonitrile-acetone interface into the hysteresis region during directional solidifications and watched for this meta-stable planar interface to spontaneously transform. Qian and Cummins [48] introduced a local heat-pulse perturbation generated from a laser-fiber coupling mechanism to investigate the response of a single succinonitrile-acetone dendrite growing by directional solidification. Later, Williams et al. [49] used the same localized thermal perturbations applied at periodic intervals to study the response of the sidebranches of pivalic acid-coumarin dendrites to periodic perturbation in directional solidification. We continue utilizing this laser perturbation method to explore the dynamics of planar-cellular morphology. Details are presented in section 4.2.

2. Theory

2.1 Mathematical Formulation

The mathematical description of directional solidification is difficult because it is a non-local, time-dependent problem, in which the temperature and solute concentration fields depend non-linearly on the interface shapes. Furthermore, the boundary conditions apply on an unknown boundary which is itself the solution (Stefan problem)[50].

The basic equations appropriate for the description of directional solidification of a dilute binary alloy at a constant speed V are those that govern heat flow, solute diffusion, the melting temperature, and solute and energy conservation at the interface.[51] It is convenient to employ a coordinate system (x, z) which moves with the steady-state interface at a speed V in the direction of solidification (which is taken as the z axis).The x axis coincides with the initial mean position of the interface at time t = 0. From Figure 3, a point with respect to the stationary coordinate has coordinate (x', z', t'), but with respect to the moving frame, its coordinates are (x, z, t). It is evident that they satisfy for time t > 0, the equation $z = \varepsilon\zeta(x,t) = z' - Vt$, $x = x'$, $t = t'$. The mean position of this interface is assumed to be moving with the constant pulling speed V in stationary (x',z') coordinates, so that

$$\lim_{z \to \infty} \frac{1}{2z} \int_{-z}^{z} \zeta(x,t)dx = 0$$

to the lowest order.[13] Thus the differential equation for diffusion, known as Fick's second law and written as $\frac{\partial c}{\partial t} = D\nabla^2 c$ in the stationary lab frame, becomes $\frac{\partial c}{\partial t} = D\nabla^2 c + V\frac{\partial c}{\partial t}$ in the reference frame of the sample which is moving in the lab frame with a velocity *V*. Furthermore, we use the following standard assumptions [12]:

-- convection in the liquid is neglected [52];

-- instantaneous local thermodynamic equilibrium on the front is assumed, which implies that the interface is rough on the microscopic scale so that kinetic effects can be neglected;

-- heat diffusion is quasi-instantaneous compared with the solute diffusion [53, 54, 55], so that all terms of the order D_L / D_{th} are neglected in equations (2.2), (2.3) and (2.7) (See later in this section). Note that this restriction will be relaxed in the complete treatment presented later in the nonlinear stability analysis.

-- solute diffusion is neglected in the solid since $D_S/D_L \sim 10^{-5}$, known as the one sided model [13, 56, 57] in contrast to the symmetric model [14,15, 58, 59, 60] in which $D_S = D_L$.

-- the temperature is fixed at the two thermal contacts, namely:

$T = T_1$ *at* $z = z_1$

$T = T_2$ *at* $z = z_2$;

-- a dilute binary alloy system which implies a phase diagram as shown in Figure 4;

-- neglecting the transverse boundary conditions, which implies that the scale of front structures is small compared with the transverse size of the sample. This assumption is justified since the size of interface deformations is usually on the order of µm while the width of the sample is on the order of mm.

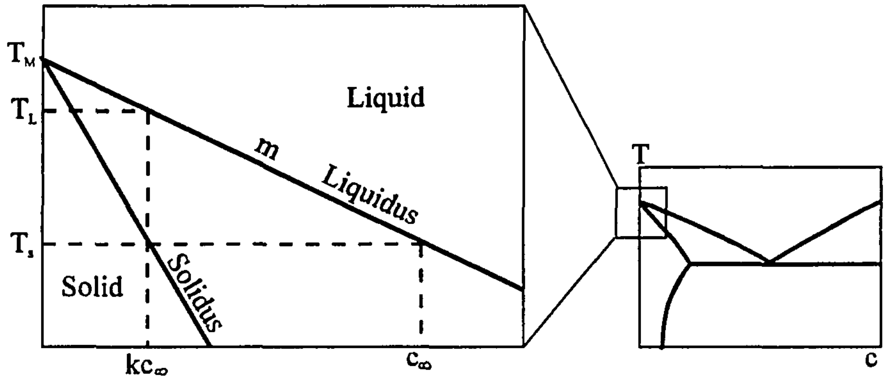

Figure 4 Low Concentration Part of the Phase Diagram of a Binary Mixture.

In writing the equations we shall use the following nomenclature:[13]

V	pulling speed (equals the constant mean steady-state velocity of the interface),
$c(c')$	concentration of the solute in the liquid (solid),
$T(T')$	temperature in the liquid(solid),
$D(D')$	diffusion coefficient of the solute in the liquid(solid),
$D_{Th.} (D_{Th.}') = K_{Th.}/C_L (K_{Th.}'/C_S)$	thermal diffusivity of liquid (solid),
$K_{th}(K_{th}')$	thermal conductivity of liquid (solid),
$C_L (C_S)$	specific heat of liquid(solid) per unit volume,
T_M	the melting temperature, in Kelvin, of the pure solvent,
d_0	σ / L capillary constant,
σ	surface free energy per unit area,
L	latent heat of fusion per unit volume,

k	partition coefficient given by the ratio of the equilibrium concentration of the solute on the solid side of the interface to that on the liquid side,
m	$dT_m(0)/dc$ slope of the liquidus line on the phase diagram,
$\mathbf{n}$	unit normal to the interface, pointing into the liquid,
$z = \varepsilon\zeta(x,t)$	equation of the solid/liquid interface having mean position $z = 0$, with ε representing a small perturbation,
κ	curvature of the interface, taken to be positive if the center of curvature is on the liquid side.

The governing differential equations, interface conditions and boundary conditions are then written as follows:

For $z > 0$ (in the liquid):

$$\frac{\partial c(x,z,t)}{\partial t} = D\nabla^2 c(x,z,t) + V\frac{\partial c(x,z,t)}{\partial z} \tag{2.1}$$

$$\frac{\partial T(x,z,t)}{\partial t} = D_{th}\nabla^2 T(x,z,t) + V\frac{\partial T(x,z,t)}{\partial z} \tag{2.2}$$

For $z < 0$ (in the solid):

$$\frac{\partial T'(x,z,t)}{\partial t} = D_{th}'\nabla^2 T'(x,z,t) + V\frac{\partial T'(x,z,t)}{\partial z} \tag{2.3}$$

The interface conditions are ($z = 0$):

$$T_i = T_i' \tag{2.4}$$

$$c_i' = k\, c_i \tag{2.5}$$

$$c_i\,(1-k)\; V\!\cdot\!\mathbf{n} = -D(\nabla c\!\cdot\!\mathbf{n})_i \tag{2.6}$$

$$LV\cdot\mathbf{n} = K_{th}\,(\nabla T'\cdot\mathbf{n})_i - K_{th}\,(\nabla T\cdot\mathbf{n})_i \qquad (2.7)$$

$$T_i = T_M + mc_i + d_0\,\kappa T_M \qquad (2.8)$$

The boundary conditions are:

$$T = T_1 \text{ at } z = z_1$$

$$T = T_2 \text{ at } z = z_2$$

and $c = c_0$ at $z = 0$

$$c = c_\infty \text{ at } z = \infty \qquad \mathbf{(2.9)}$$

2.2 Thermodynamic Stability Analysis

2.2.1 The Planar Stationary Interface Solution

As a starting point, we study a flat interface which moves at a constant velocity V having achieved steady state conditions. In the reference frame of the material (the moving frame as described in Figure 3, one can write the following diffusion equations and interface conditions following equations (2.1) to (2.9):

$$\frac{d^2c}{dz^2} + \frac{V}{D}\frac{dc}{dz} = 0 \qquad (z>0) \qquad (2.10)$$

$$\frac{d^2T}{dz^2} + \frac{V}{D_{th}}\frac{dT}{dz} = 0 \qquad (z>0) \qquad (2.11)$$

$$\frac{d^2T'}{dz^2} + \frac{V}{D'_{th}}\frac{dT'}{dz} = 0 \qquad (z<0) \qquad (2.12)$$

$$T_i = T_i' \qquad (2.13)$$

$$c_i' = k\, c_i \tag{2.14}$$

$$V c_i' (1-k) + D\, (dc/dz)_i = 0 \tag{2.15}$$

$$LV = K_{th}' (\frac{dT'}{dz})_i - K_{th} (\frac{dT}{dz})_i \tag{2.7}$$

$$T_i = T_M + m\, c_i \tag{2.17}$$

With the Boundary conditions:

$$T = \begin{cases} T_1 & (z = z_1) \\ T_2 & (z = z_2) \end{cases} \quad \text{and} \quad c = \begin{cases} c_0 & (z = 0) \\ c_\infty & (z = \infty) \end{cases} \tag{2.18}$$

2.2.2 Solving for the Concentration Field Ignoring Latent Heat

We first solve for the solute diffusion field ignoring the latent heat L. From equation (2.10), we have the general solution:

$$c = A + B \exp[-(V/D)z] \qquad (z>0) \tag{2.19}$$

where A, B are constants to be determined.

Considering the boundary conditions

$$c_{z\to 0} = c_0, \qquad c_{z\to\infty} = c_\infty$$

We then have

$$c(z) = c_\infty + (c_0 - c_\infty) e^{-(V/D)z} \tag{2.19a}$$

substituting (2.19a) into (2.15), one derives

$$c_0 = c_\infty / k \tag{2.19b}$$

hence,

$$c(z) = c_\infty (1 + \frac{1-k}{k} e^{-(V/D)z}) \tag{2.19c}$$

The solute concentration profile across the moving planar interface is shown in Figure 5. For dilute binary mixtures, solubility in the solid is usually lower than that in the liquid. The equilibrium concentrations differ by a factor of *k*, called the partition coefficient. At steady state there is a concentration jump across the interface. As the sample is being pulled at a constant velocity *V*, the solid side will reject solute into the liquid side, thus generating a concentration "spike" on the liquid side of the interface.

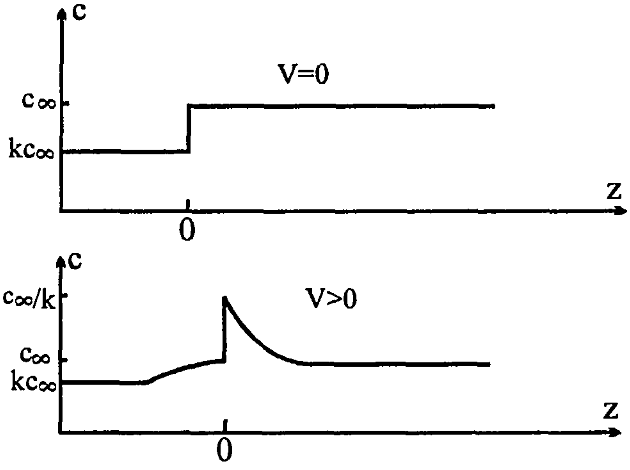

Figure 5 Concentration profile for a steady planar interface.

In the above calculation, we directly solved for the concentration field in the absence of latent heat. In other words, we assumed that K_{th} (K_{th}') is large or equivalently the latent heat L is small and can be neglected. This approximation is valid if we assume that thermal diffusion is much faster than chemical diffusion. It is a very good approximation for concentrated samples or low pulling speeds. The thermal field in the liquid will have a uniform temperature gradient (*G* is constant) along the *z* direction. This result can be readily derived from equation (2.11), (2.12) and (2.16), which imply that

$$\frac{d^2T}{dz^2} = 0,$$

So, the temperature field on the liquid side is

$$T = T_0 + G\,z \tag{2.20}$$

where $T_0 = T_M + mc$. This is the external temperature field imposed on the sample.

Next, we can evaluate the local melting temperature $T(z)$ of the sample, again neglecting the latent heat, by combining equations (2.17) and (2.19c):

$$T_m(z) = T_M + m\,c(z) = T_M + m\,c_\infty[1 + (1-k)/k\,e^{-(V/D)z}] \tag{2.21}$$

We can then plot the temperature field $T(z)$ and the local melting temperature $T_m(z)$:

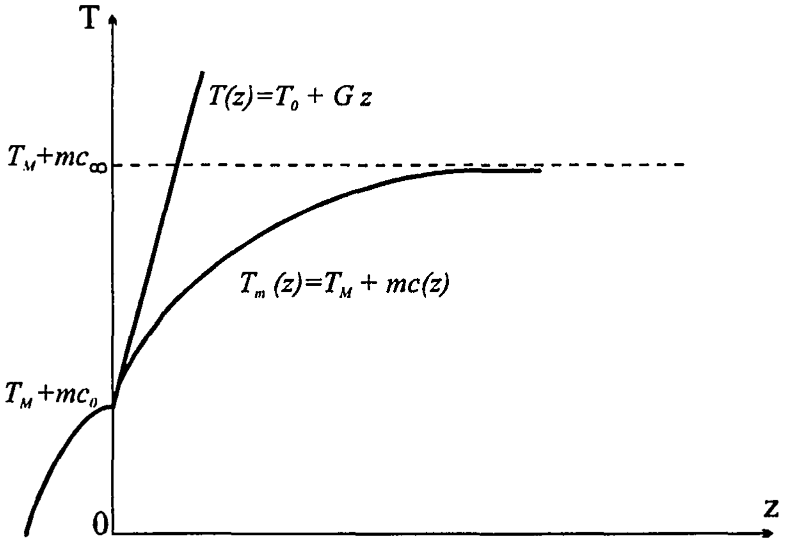

Figure 6 Applied temperature field $T(z)$ and the local melting temperature $T_m(z)$ in the sample.

The straight line in Figure 6 is the externally applied temperature field on the sample $T(z)$ (Equation (2.20)) and the curve $T_M + m\,c(z)$ represents the local melting temperature $T_m(z)$ of the sample (Equation (2.21)). When increasing the pulling speed V, the system needs a larger concentration gradient to drive the rejected solute forward into the liquid, so the initial slope of $T_m(z)$ will increase. By increasing the pulling speed V (or equivalently decreasing the temperature gradient G, the $T(z)$ line will eventually dip below the $T_m(z)$ curve. In this situation, the liquid immediately ahead of the interface is at a lower temperature than the local freezing temperature for its concentration, and is therefore thermodynamically unstable. This is the so-called "constitutionally supercooled" state. Furthermore, this supercooled liquid is in contact with the solid, so there is no barrier to nucleation. As a result, the planar interface will be destroyed and instabilities will occur. Note that the interface is located at $z = 0$ where the slope of the $T_m(z)$ curve is a maximum. So, thermodynamic stability requires:

$$G \geq \left. \frac{dT_m(z)}{dz} \right|_{z=0} = m \left. \frac{dc(z)}{dz} \right|_{z=0} \tag{2.22}$$

Combining equations (2.19a), (2.21) and (2.22) leads to the so called "constitutional supercooling" criterion and gives a critical velocity V_c above which the thermodynamic instability occurs (at a given solute concentration and temperature gradient):

$$V_c = \frac{GDk}{(1-k)mc_\infty} \tag{2.23}$$

as first proposed by Tiller, et al [61]

There are three variables in equation (2.23): the pulling speed V, the solute concentration c_∞, and the temperature gradient G. Experimentally, the temperature gradient G is usually fixed and V, c are the parameters that are varied. For a given temperature gradient, the critical velocity is higher for a dilute sample than for a concentrated sample. For $V<V_C$, the planar interface is always stable; for $V>V_C$ it is unstable.

2.2.3 Solving for the Thermal Field Including Latent Heat

In the previous section we have ignored the effects of latent heat. Although this is a good approximation for low pulling speeds and high concentrations it is not valid for high pulling speeds and low concentrations where the effects of latent heat can become important.

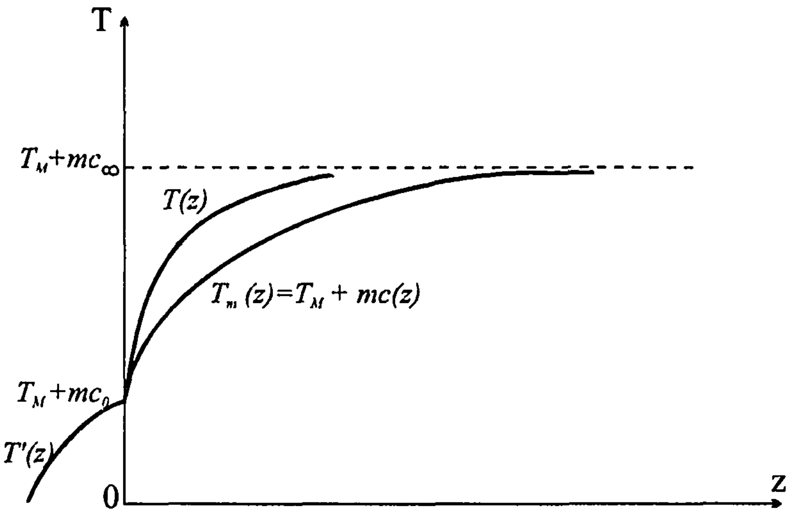

Figure 7 Temperature field *T(z)* and local melting temperature $T_m(z)$ with the latent heat included.

Similar to the above solution for the concentration field, the thermal field can be found from equations (2.11) and (2.12) subject to the boundary condition (2.18):

$$T = T_0 + \frac{T_1 - T_0}{1 - e^{-(V/D_{th})z_1}}\left(1 - e^{-(V/D_{th})z}\right) \quad (z>0) \qquad (2.24)$$

$$T' = T_0 + \frac{T_1 - T_0}{1 - e^{-(V/D_{th}')z_1}}(1 - e^{-(V/D_{th}')z}) \quad (z<0) \qquad (2.25)$$

Without latent heat the temperature is linearly related to the position z (as shown in Figure 6). But equation (2.24) shows that the temperature field in the sample is no longer characterized by a constant gradient because of the latent heat of solid/liquid fusion. (See Figure 7).

Since z_1, z_2 are not fixed quantities, only the gap between cold and hot contact l is a fixed length:

$$l = z_1 - z_2 \qquad (2.26)$$

For simplicity, let's assume $K_{th}' = K_{th}$, $D_{th}' = D_{th}$. And, we also have

$$T_0 = T_M + mc_0 = T_M + mc_\infty/k \qquad (2.27)$$

Putting equations (2.24) - (2.27) into the interface condition (2.16), we find

$$\frac{LD_{th}}{K_{th}} = \frac{T_2 - T_M - mc_\infty / k}{1 - e^{-(V/D_{th})z_1} e^{(V/D_{th})l}} - \frac{T_1 - T_M - mc_\infty / k}{1 - e^{-(V/D_{th})z_1}} \qquad (2.28)$$

Thermodynamic stability requires that:

$$\left.\frac{dT(z)}{dz}\right|_{z=0} \geq \left.\frac{dT_m(z)}{dz}\right|_{z=0}$$

i.e.

$$\frac{T_1 - T_0}{1 - e^{-(V/D_{th})z_1}} \cdot \frac{V}{D_{th}} \geq \frac{mc_\infty(1-k)}{kD} \qquad (2.29)$$

From equations (2.28) and (2.29), one can eliminate the quantity z_1 and obtain the critical velocity V_C.

$$V_C = \frac{D_{th}}{l} \cdot \ln \left[\frac{1 - \dfrac{T_2 - T_0}{LD_{th}/K_{th} + mD_{th}c_\infty (1-k)/(kD)}}{1 - \dfrac{T_1 - T_0}{mD_{th}c_\infty (1-k)/(kD)}} \right] \tag{2.30}$$

As mentioned earlier, for concentrated samples at low pulling speeds, chemical diffusion is dominant and latent heat can be neglected since heat diffusion is much faster than chemical diffusion. But for low concentration samples at high pulling speeds, the latent heat plays an important role in determining the critical condition for thermodynamic instability.

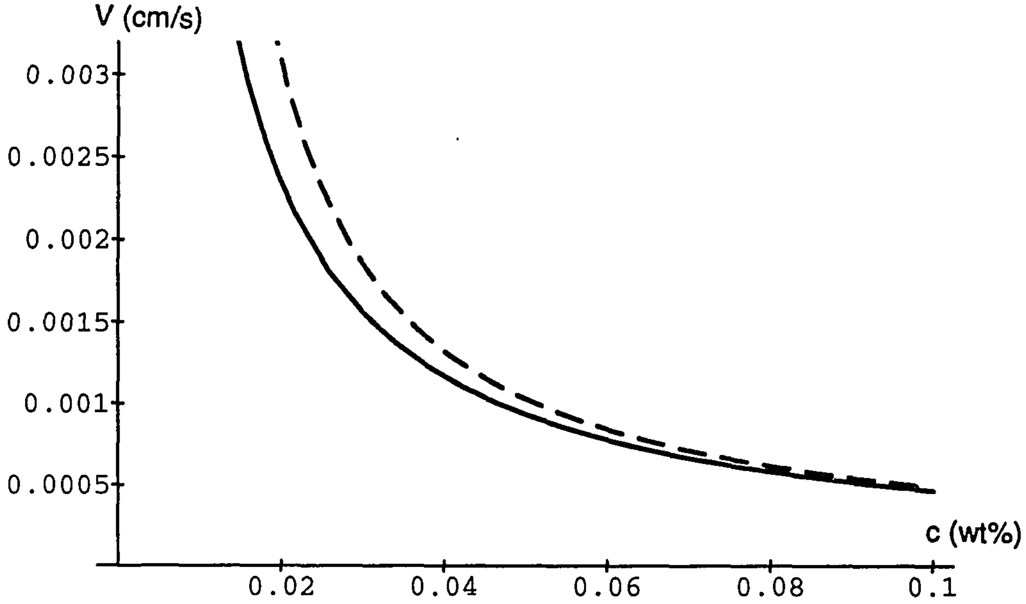

Figure 8 Critical velocity V_C vs concentration c for SCN/Acetone at G=100K/cm with (dashed line) and without (solid line) latent heat.

Figure 8 shows the critical velocities resulting from the chemical diffusion calculation both excluding and including the effects of the latent heat L. It indicates that the latent heat effects become significant for low solute concentration samples and at high pulling speed. The result without latent heat (solid line) approached $V=\infty$ asymptotically as $c \rightarrow 0$, i.e. there is always a critical velocity for any concentration. With latent heat included, however, there is no instability for very low concentrations.

2.3 Linear Stability Analysis: The Mullins - Sekerka Instability

The constitutional supercooling criterion gives a necessary condition for a planar interface to be thermodynamically unstable, but reveals nothing about the spatial structure resulting from the instability. To go further a dynamic stability analysis is required. Mullins and Sekerka [10] in 1964 first calculated the linear stability of a planar interface to infinitesimal perturbations.

Following Mullins and Sekerka, again neglecting the efffects of latent heat, we consider a single sinusoidal perturbation [58, 62] to the steady state planar interface $z_i = 0$ of the form $A(t)\ \zeta(x)$, i.e.:

$$A_0 Cos(qx)e^{a_0 t}$$

The interface position will now be

$$z_i = 0 + A_0 Cos(qx)e^{a_0 t} = A_0 Cos(qx)e^{a_0 t} \tag{2.31}$$

We assume that the impurity concentration field will be affected infinitesimally and with the same x dependence:

$$\begin{aligned} c &= c_0 + B(z)\ Cos(qx)\ e^{a_0 t} \\ &= c_\infty\left(1+\frac{1-k}{k}e^{-(V/D)z}\right)+B(z)Cos(qx)e^{a_0 t} \end{aligned} \tag{2.32}$$

where $a_0(q)$ is referred to as the linear gain coefficient, i.e. the growth rate of the instability satisfying $\frac{dA}{dt} = a_0 A$, where q is the wavenumber of the perturbation and A_0 and $B(z)$ are to be determined.

Substituting (2.32) back into equation(2.1), one finds:

$$\frac{d^2B(z)}{dz^2}+\frac{V}{D}\cdot\frac{dB}{dz}-\left(\frac{a_0}{D}+q^2\right)B(z)=0 \tag{2.33}$$

A general solution for B(z) can be written as:

$$B(z) = B_0 e^{-\lambda z} \tag{2.33a}$$

Combining equations (2.33a) and (2.33), one finds that λ obeys the following equation:

$$\lambda^2-\frac{V}{D}\cdot\lambda-\left(\frac{a_0}{D}+q^2\right)=0 \tag{2.33b}$$

Hence,

$$2\lambda l_D=\left[1+\sqrt{1+4\left(\frac{a_0}{D}+q^2\right)l_D^2}\right] \tag{2.33c}$$

where $l_D = V/D$, is the impurity diffusion length.

Since we are assuming a uniform temperature gradient G on the liquid side, one can write:

$$T = T_0 + G z = T_M + m c_0 + G z$$

Then combining with the Gibbs-Thompson relation--interface condition (2.8):

$$T_M + m c_0 + G z_i = T_M + m c_i + d_0 k T_M \tag{2.34}$$

Yielding:

$$c_i = c_0 + G\, z_i / m + d_0\, kT_M / m \tag{2.34a}$$

Next, substitute expressions (2.31), (2.32) and (2.33a) into equation (2.34a) and the interface condition (2.6), and keeping only the leading terms of the Taylor expansion, omitting terms of order $O(A^2)$, $O(B^2)$ and $O(AB)$, finally, by eliminating the constant coefficients A_0 and B_0, yields [63]:

$$\frac{a_0 l_D^2}{D} = (\lambda l_D + k - 1)\cdot(1 - \frac{l_D}{l_T} - d_0 l_D^2 q^2) - k \tag{2.35}$$

where

$$l_T = \frac{\Delta T}{G} = \frac{m c_\infty (1-k)}{kG} \tag{2.36}$$

is referred as the thermal length.

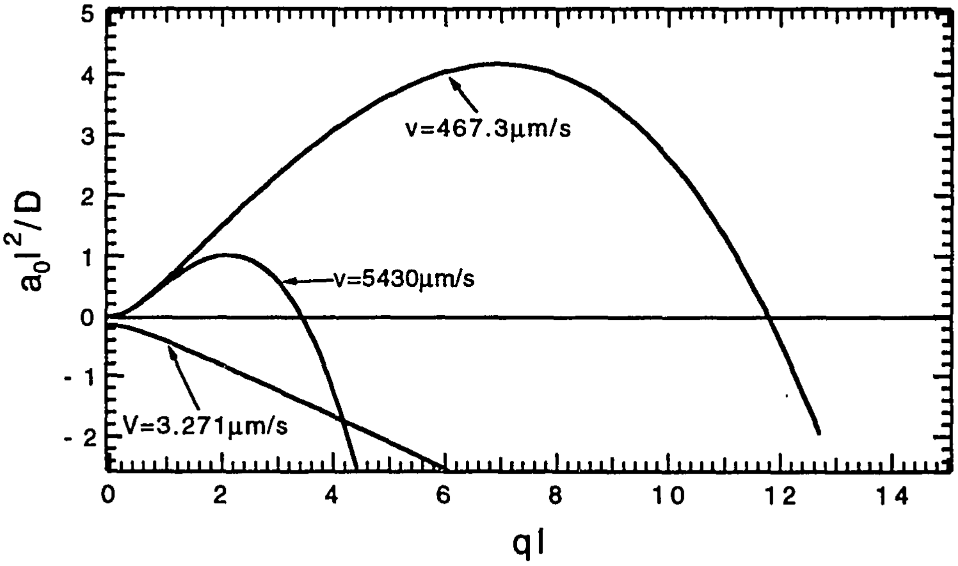

Figure 9 Dimensionless growth rate $a_0 l^2/D$ vs dimensionless wavenumber ql under the quasi-stationary approximation. (SCN/Acetone, G=100K/cm, c=0.1 wt%)

Equation (2.35) is the dispersion relation between the linear growth rate a_0 and the perturbation wave number q. Plots of the dimensionless quantity $a_0 l^2/D$ vs ql and the linear growth rate a_0 vs q are shown below: (Figure 9 and Figure 10)

We have adopted a quasi-stationary approximation in plotting Figure 9, i.e. choosing $a_0 = 0$ in equation (2.33c). Figure 10 shows the result obtained without the quasi-stationary approximation, obtained by solving equations (2.33c) and (2.350 self-consistently.

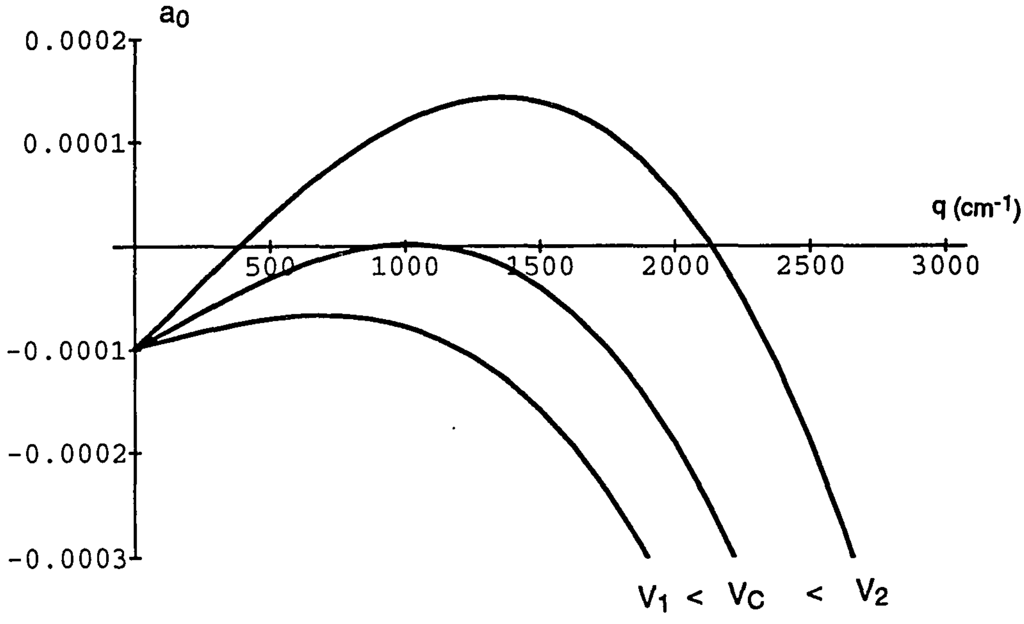

Figure 10 The linear growth rate a_0 vs the perturbation wave number q without the quasi-stationary approximation. (SCN/C152, G=100 K/cm, c=0.1 wt%)

Figures 9 and 10 showed several curves for different values of V. From the plots, one can see that the system is stable ($a_0<0$) at small V and is unstable ($a_0>0$) against infinitesimal perturbations as V becomes larger. In fact, there are three variables involved:

c, G and V. In directional solidification experiments, the concentration c and temperature gradient G are usually fixed and the velocity V is varied. As V is increased, the curve will eventually cross the horizontal axis, positive values of a_0 result and there is a band of unstable deformations. The width of this band of unstable deformations initially increase and will eventually decrease as the pulling speed becomes sufficiently large, taking the system to absolute stability.

The above Mullins-Sekerka stability analysis consists of a computation of the linear growth rate a_0 of sinusoidal perturbations to the flat interface. This analysis yields the linear growth rate a_0 for a given mode of wave number q as a function of the control parameters from equations (2.35) and (2.33c). As long as this rate is negative, the perturbation cannot grow, whereas it will grow if a_0 is positive. The loci where the growth rate is zero (i.e. where $a_0 = 0$), define a curve in the control parameter-wave number plane called the neutral stability curve: for a given value of the control parameter above onset, there is a band of modes with non-negative growth rates (a_0), as depicted in (V,q) space in Figure 11. Note that the curve is closed so that there is also an upper critical velocity V_{max}, also called the absolute maximum velocity, above which the planar interface is again stable.

The lowest speed at which the planar interface is unstable is V_C, the minimum of this curve. The maximum absolute velocity (restablization velocity) is given by [8] (see also section 2.4.3.1 for a detailed derivation):

$$V_{\max} = \frac{Dmc_{\infty}(1-k)}{d_0 T_M k} \qquad (2.37)$$

The dotted line represents the fastest growing mode(most unstable mode). It corresponds to the maximum of the $a_0(q)$ curve, i.e. to $\partial a_0 / \partial q = 0$.

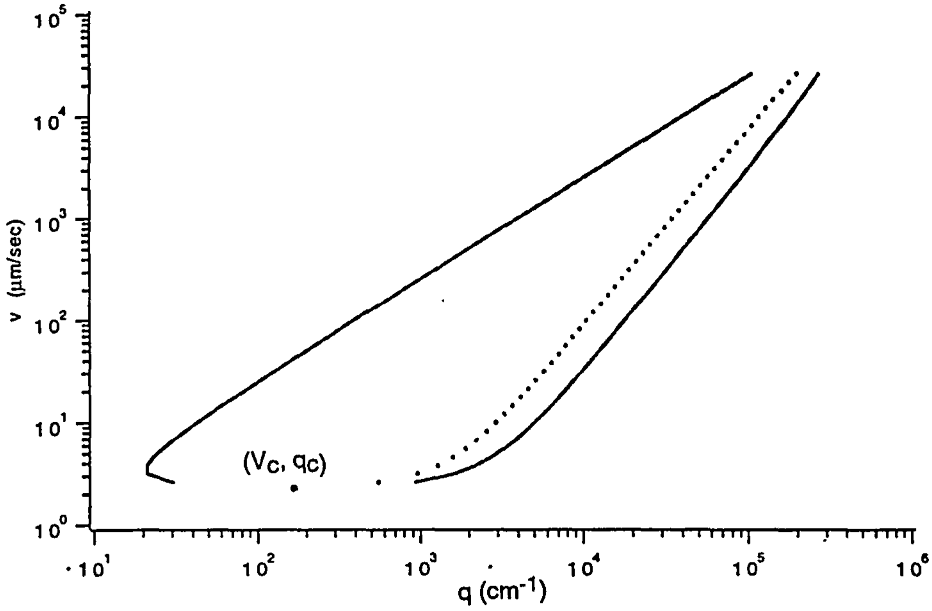

Figure 11 Neutral stability curve.(SCN/Acetone, G=52 K/cm, c=0.1wt%)

To further illustrate the existence of the initial instability and re-stabilization predicted by the linear theory, we solve for the fastest growing mode $q_0 = q_0(c,V,G)$ by taking the derivative of equation (2.35), $\frac{\partial a_0}{\partial q} = 0$. Then substituting $q_0 = q_0(c,V,G)$ back into equation (2.35), we get the linear growth rate a_0 against the control parameters c, V, G for the fastest growing mode. As shown in Figure 12 for a SCN/Acetone mixture, at a certain concentration c and temperature gradient G, the interface is stable ($a_0<0$) when the pulling speed is either sufficiently low or above V_{max}.

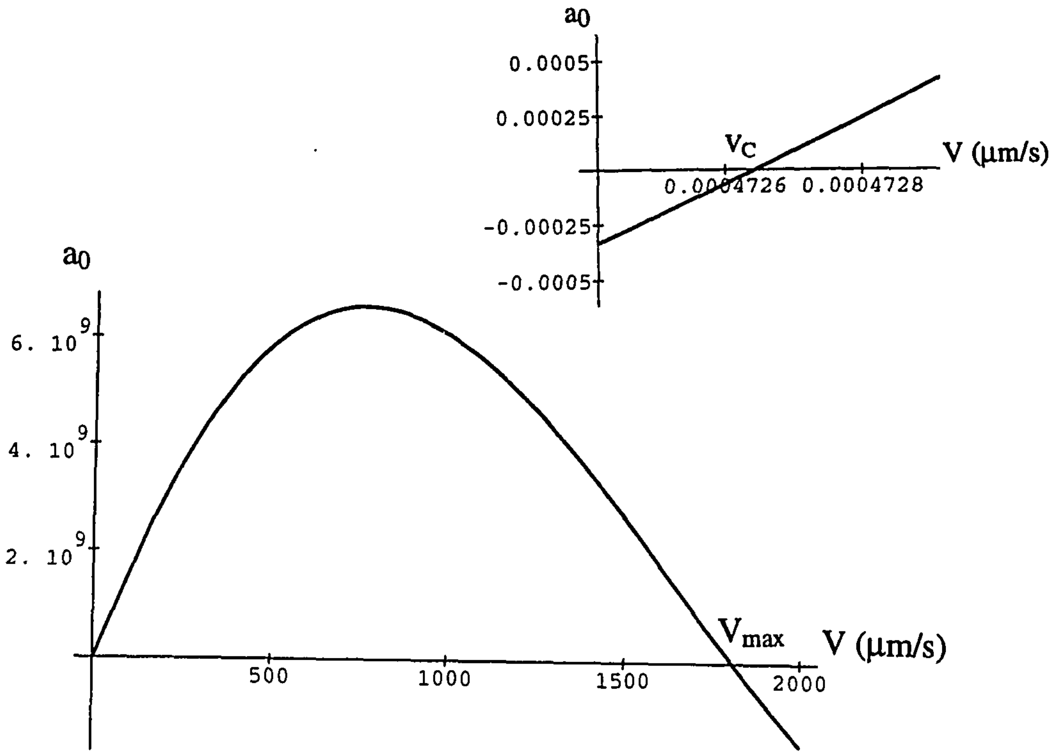

Figure 12 The linear growth rate a_0 vs pulling speed V. (SCN/Acetone, G=100K/cm, c=0.1 wt%). The initial critical velocity V_C and the restablization velocity V_{max} are indicated on (a) and (b) respectively.

On the other hand, we can also plot the neutral stability curve, obtained by eliminating a_0 and q from the marginal stability conditions of $a_0 = 0$ and $\frac{\partial a_0}{\partial q} = 0$ of equation (2.35), in the control parameter (c, V, G) plane. Figures 13 and 14 show G vs V at a fixed concentration, and V Vs c at a given temperature gradient G, respectively.

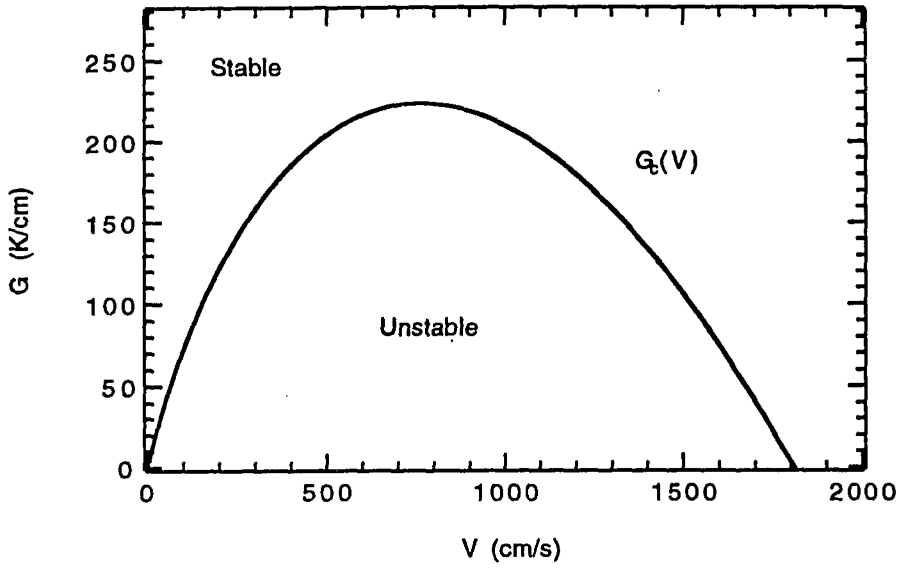

Figure 13 Marginal stability curve in the *G-V* plane. (SCN/Acetone, *c*=0.1 wt%)

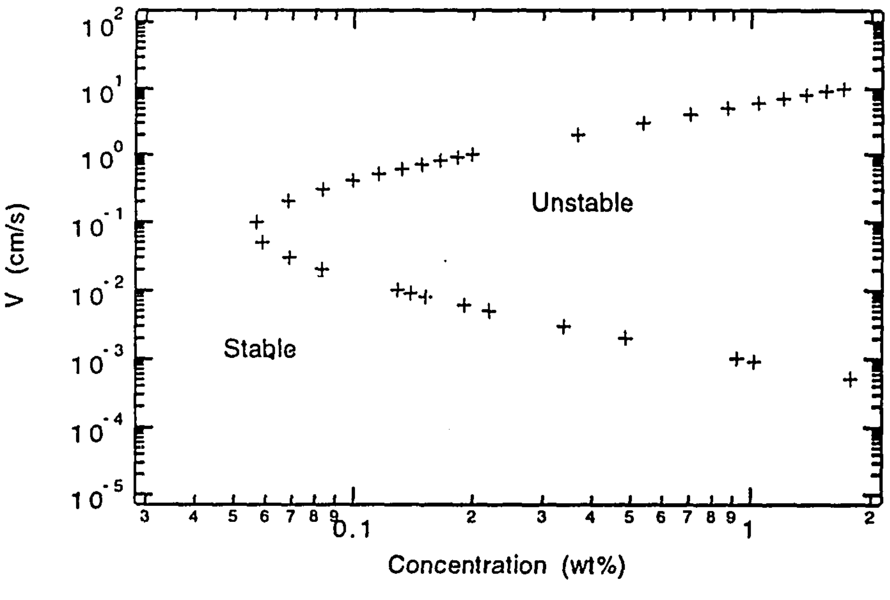

Figure 14 Marginal stability curve in the *V-c* plane. (parameters are for SCN/Acetone at *G*=100 K/cm, except that we take *k*=0.5 for simplicity)

On both figures, the inside regions of the curves correspond to instability, outside corresponds to stability. They also clearly indicate the initial instability as well as the restablized velocity or temperature gradient above which the system regains stability. Note that, as illustrated in Figure 14, the upper and lower critical velocities approached each other as the concentration is decreased. Also, in contrast to the thermodynamic analysis (constitutional supercooling criterion), the dynamical analysis shows that, even without considering latent heat, no instability will occur for concentrations below the "nose" of the curve in Figure 14.

2.4 Nonlinear Stability Analysis

2.4.1 Nonlinear Stability Analysis and the Amplitude Equation

The preceding linear stability analysis predicts critical values of the control parameters for the onset of instability; that is, values of the parameters such that infinitesimal disturbances of the proper wavelength (single mode approximation) will initially grow exponentially with time. However, it doesn't deal with the processes by which the bifurcation from a planar to a wavy interface occurs or what happens once the instability occurs. It cannot describe the evolution of the unstable planar interface to a nonplanar, cellular interface, since, due to the exponential temporal growth of the perturbations, the higher order terms that are neglected in order to obtain the linear perturbation equations become comparable in magnitude to the terms that are retained. To go further, one has to perform a nonlinear stability analysis to take into account the response of the interface to finite amplitude perturbations. This calculation is only reliable close to the onset of the instability, where the band of unstable modes is still narrow, because the linear superposition of modes does not generally apply in a nonlinear analysis.

Theoretical treatments of the nonlinear problem may be divided into two broad categories.[64] The first category consists of expansion methods that are intended to provide nonplanar solutions for small, but finite, amplitudes in a limited region near the critical conditions. The solution is generally represented as an asymptotic expansion, with each term in the expansion of higher order in the expansion parameter than the preceding one. The second category is composed of numerical solutions to the full nonlinear equations. Although the numerical solutions may have broader range in surveying parameter space, the expansion method provides a more explicit description of the dependence of the solution on the governing parameters. Hence, the theoretical procedures carried out in this thesis were adapted to the expansion method as presented in reference 12 and 13.

The nonlinear stability calculation yields an equation for the time derivative of the amplitude with wave number q in the Landau form:

$$d\zeta_q/dt = a_0\, \zeta_q - a_1\, \zeta_q^3 - a_2\, \zeta_q^5 + \text{higher order terms} \qquad (2.38)$$

Like any expansion, this equation cannot be valid beyond the vicinity of the bifurcation where ζ_q is small and $(q - q_c)/q_c \ll 1$. The first term on the right hand side of equation (2.38) comes from the linear stability analysis discussed above and the coefficient a_0 is equal to the linear growth rate a_0 of the last section. Since it may vanish at the bifurcation, its q-dependence must be taken into account. However a_1 is usually finite, so one can neglect its q-dependence and take its value at the bifurcation. Of course, when a_1 vanishes, one has to extend equation (2.38) to the next non-zero term (fifth order term). For a full description of the different possible behaviors, depending upon the signs of a_0 and a_1, four cases must be considered:

(1) $a_0 < 0$ and $a_1 > 0$. The planar front is the only solution; the nonlinear term stabilizes the interface.

(2) $a_0 > 0$ and $a_1 > 0$. The planar front is unstable and the mode begins to grow exponentially. Since a_1 is positive, the instability saturates to a stable solution of finite amplitude: $\zeta_q = (a_0/a_1)^{1/2}$. Close to the bifurcation, one can show that $a_0(\zeta_q) \propto (V - V_C)$. Hence the amplitude of the deformation of wave number q grows as $(V - V_C)^{1/2}$ analogous to a second-order phase transition where the amplitude would be the order parameter. This bifurcation which occurs as a_0 changes from $a_0 < 0$ to $a_0 > 0$ is called supercritical (it is also referred to by many other names, e.g. forward bifurcation, normal bifurcation, pitchfork bifurcation, etc.; it is analogous to a second order transition).

(3) $a_0 < 0$ and $a_1 < 0$. Although the linear stability analysis predicts a stable planar interface, a finite amplitude destabilized interface $\zeta_q = (a_0/a_1)^{1/2}$ is also a solution. Since the interface is unstable, a finite jump from a planar interface to a destabilized one may occur at a velocity below the critical velocity given by the linear analysis. This bifurcation is similar to a first order transition and is called subcritical (it is also referred to as backward or inverted bifurcation).

(4) $a_0 > 0$ and $a_1 < 0$. Destabilization is enforced by the nonlinear term, thus higher order terms have to come into play, e.g. an additional term of $a_2\zeta_q^5$. This provides a finite-amplitude steady state.

A bifurcation diagram for the amplitude ζ_q of the interface Vs its velocity is shown schematically in Figure 15.

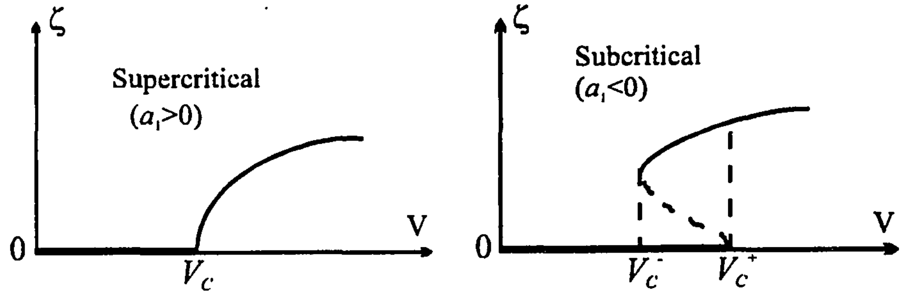

Figure 15 Schematic bifurcation diagrams. For the subcritical case, the planar and cellular interface are both solutions for $V_c^- \leq V \leq V_c^+$.

One has to calculate a_l in order to predict if the bifurcation should be subcritical or supercritical. This calculation, which involves unwieldy formulae, was first performed by Wollkind and Segel(1970) [13] for the one-sided model, i.e. assuming $\eta = D'/D = 0$, by Langer and Turski (1977) [14] and Ungar and Brown (1984) [15] for the symmetric model, i.e. $\eta = 1$, $n = K_{th}'/K_{th} = 1$, and was extended by Caroli et al. [12] to the two sided model with $0<\eta<1$ (This paper contained a minor error, subsequently corrected by Wollkind et al.(1986)[65], which does not change the qualitative conclusions). Caroli et al.(1982) [12] found that for V and G both small, in the high-concentration case where the thermal conductivities are equal and latent heat can be neglected, the nature of the bifurcation strictly depends on the material via the value of the partition coefficient k. For $k > 0.45$, $a_l>0$ and the bifurcation is supercritical; for $k < 0.45$, $a_l < 0$ and the bifurcation is subcritical.

Alexander et al. [24] (1986) included the latent heat in the condition describing the local balance of energy across the moving surface of discontinuity, carried out a complete nonlinear analysis, and solved for the Landau coefficient a_1 with latent heat included.

In this section, I will review the non-linear extension of the Mullins-Sekerka analysis for one-dimensional deformations, using a perturbation expansion.[13,12,65] There are two major mathematical methods used in treating this weakly nonlinear analysis. One is the adjoint operator method and the other is a so called direct method. Although both methods yield the same Landau coefficients, the latter treatment is more intuitive. Furthermore if both the Landau coefficient and a solution to the equations are required, the direct method is superior. We shall adopt this approach which involves the consideration of a two-dimensional disturbance which has the small spatial dependence with wave number q as the marginally stable mode (predicted by the linear theory) but has an unknown amplitude $\varepsilon\zeta$. Owing to the inherent non-linearities, the superposition principle, which allows the separate treatment of each infinitesimal amplitude disturbance, no longer applies. Thus we are constrained to examine the non-linear behavior of a single critical disturbance and its self-iteration.

2.4.2 Scaling, Dimensionless Parameters and the Governing Equations

At a starting point, we use the standard approximation as mentioned in section 2.1 but use a more general model -- two-sided model [12], i.e. $\eta = \frac{D'}{D} \neq 0 \text{ or } 1,\ n = \frac{K_{th}'}{K_{th}} \neq 1$.

Rather than handling the basic dynamic equations of (2.1)-(2.9) as written, it is common practice to rescale the variables in order to obtain a set of dimensionless equations. We use the following scaling factors:

length scale: $\frac{D}{V}$

time scale: $\frac{D^2}{V}$

concentration scale: $c^*(0)$

temperature scale: T_M

where $c^*(0)$ is the concentration on the liquid side of the interface for the planar stationary solution.

We now introduce the following dimensionless variables:

Physical Variables	Dimensionless Variables
$\underline{c}$	$c = \frac{\underline{c}}{c^*(0)}$
$\underline{c}'$	$c' = \frac{\underline{c}'}{c^*(0)}$
$\underline{T}$	$T = \frac{\underline{T}}{T_M}$
$\underline{T}'$	$T' = \frac{\underline{T}'}{T_M}$
$(\underline{x}, \underline{z})$	$(x, z) = \frac{(\underline{x}, \underline{z})}{(D/V)}$

$$\underline{\zeta} = \varepsilon\underline{\zeta} \qquad\qquad z = \varepsilon\,\zeta = \frac{\varepsilon\underline{\zeta}}{(D/V)}$$

$$\underline{t} \qquad\qquad t = \frac{\underline{t}}{(D/V^2)}$$

and define the following parameters:

$$\gamma = \frac{d_0}{D/V} = \frac{\sigma V}{LD}\ ,$$ scaled capillary length;

$$M = \frac{c_0^{*}(0)}{T_M} \cdot (d\underline{T}/d\underline{c})_{T=T_M}\ ,$$ scaled liquidus slope;

$$n = \frac{K_{th}'}{K_{th}},\quad \eta = \frac{D'}{D},\quad \zeta_x = \frac{\partial\zeta}{\partial x}\ ,\quad \zeta_{xx} = \frac{\partial^2\zeta}{\partial x^2}\ ,\quad \zeta_t = \frac{\partial\zeta}{\partial t}\ .$$

Note that underlined variables are introduced to distinguish the physical variables (underlined) from dimensionless variables in the above definition. Substituting the physical quantities defined with those of dimensionless correspondents in the governing equations (2.1)-(2.9), we can write them in a dimensionless form: but, for simplicity in writing, I will ignore the underlines in physical parameters. From now on, all the variables are dimensionless unless otherwise indicated, so the following equations (2.39)-(2.48) (dimensionless) should not be confused with (2.1)-(2.9) in section 2.1 (they are physical parameters!):

For z > εζ (in the liquid):

$$\nabla\ c(x,z,t) + \frac{\partial c(x,z,t)}{\partial z} - \frac{\partial c(x,z,t)}{\partial t} = 0 \tag{2.39}$$

$$\nabla\ T(x,z,t) = 0 \tag{2.40}$$

For z < εζ (in the solid):

$$\eta\nabla\; c'(x,z,t) + \frac{\partial c'(x,z,t)}{\partial z} - \frac{\partial c'(x,z,t)}{\partial t} = 0 \qquad (2.41)$$

$$\nabla\; T'(x,z,t) = 0 \qquad (2.42)$$

The interface conditions (at $z = \varepsilon\zeta$):

temperature continuity:

$$T = T' \qquad (2.43)$$

local phase equilibrium:

$$c' = k\,c \qquad (2.44)$$

concentration balance:

$$\frac{\partial c}{\partial z} - \eta\frac{\partial c'}{\partial z} - \varepsilon\zeta_x\left(\frac{\partial c}{\partial x} - \eta\frac{\partial c'}{\partial x}\right) = (k-1)c(1+\varepsilon\zeta_t) \qquad (2.45)$$

energy conservation:

$$n\frac{\partial T'}{\partial z} - \frac{\partial T}{\partial z} - \varepsilon\zeta_x\left(n\frac{\partial T'}{\partial z} - \frac{\partial T}{\partial z}\right) = \frac{LD}{T_M K_{th}}(1+\varepsilon\zeta_t) \qquad (2.46)$$

interface temperature shift due to concentration and surface tension energy (Gibbs-Thomson relation):

$$T = 1 + M c + \gamma\,\varepsilon\,\zeta_{xx}\,(1 + \varepsilon^2\,\zeta_x^2)^{-3/2} \qquad (2.47)$$

the boundary conditions are:

$$T = \begin{cases} T_1 & (z = z_1) \\ T_2 & (z = z_2) \end{cases} \quad \text{and} \quad c = \begin{cases} 1 & (z = 0) \\ k & (z = \infty) \end{cases} \qquad (2.48)$$

To obtain equations (2.40) and (2.42), we have assumed that heat diffusion is quasi-instantaneous compared with solute diffusion so that all terms of order D/D_{th} are neglected. Some algebraic details of the derivation of equations (2.39)-(2.47) is given in Appendix A.

2.4.3 The Nonlinear Problem Ignoring Latent Heat

2.4.3.1 The Planar Interface and the Linear Stability Solution

Utilizing the dimensionless equations given in the preceding section, the planar stationary and the linear stability results can also be readily obtained. But since latent heat is neglected, equation (2.46) becomes

$$n\frac{\partial T'}{\partial z}-\frac{\partial T}{\partial z}-\varepsilon\zeta_x(n\frac{\partial T'}{\partial z}-\frac{\partial T}{\partial z})=0 \tag{2.46a}$$

Under the steady state conditions, one can set the time derivative terms to be zero in equations (2.39)-(2.42) and combining with the interface and boundary conditions (2.43)-(2.48), one can easily solve for the planar stationary solutions:

For $z>0$,

$$c_0(z) = 1+ (k-1)\,(1 - e^{-z}) \tag{2.49}$$

$$T_0(z) = 1 + M + G\,z \tag{2.50}$$

For $z<0$,

$$c_0'(z) = k \tag{2.51}$$

$$T_0'(z) = 1 + M + \frac{G}{n}z \tag{2.52}$$

where

$$G = \frac{T_l - 1 - M}{z_l} \tag{2.53}$$

and

$$\frac{z_1}{-z_2} = n\frac{T_2 - 1 - M}{T_1 - 1 - M} \tag{2.54}$$

Figures 16 and 17 show the scaled solute concentration field and the scaled temperature field of a binary mixture, respectively.

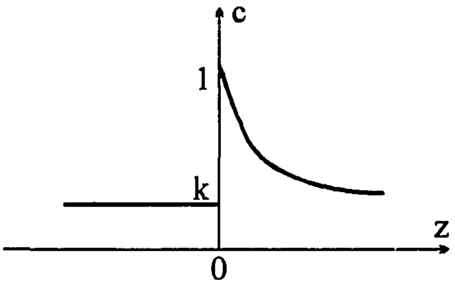

Figure 16 Scaled concentration field.

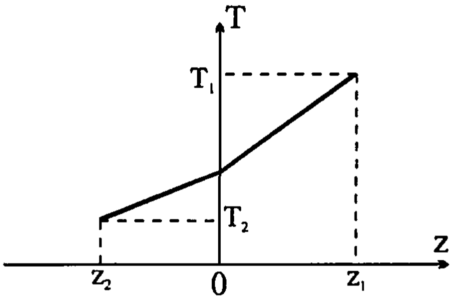

Figure 17 Scaled temperature field.

Proceeding according to the Mullins-Sekerka linear stability analysis discussed in section 2.3, we investigate the stability of a planar front which undergoes a small harmonic deformation by considering solutions of the form

$$v\,(x,\, z,\, t;\, e) = v_0\,(z) + v_{11}(x,\, z,\, t,\, e) \tag{2.55}$$

or equivalently

$$\begin{bmatrix} c(x,z,t;\varepsilon) \\ c'(x,z,t;\varepsilon) \\ T(x,z,t;\varepsilon) \\ T'(x,z,t;\varepsilon) \\ \varepsilon\zeta(x,t;\varepsilon) \end{bmatrix} = \begin{bmatrix} c_0(z) \\ c_0'(z) \\ T_0(z) \\ T_0'(z) \\ 0 \end{bmatrix} + \begin{bmatrix} c_{11}(z) \\ c_{11}'(z) \\ T_{11}(z) \\ T_{11}'(z) \\ \zeta_{11} \end{bmatrix} Cos(qx)e^{a_0 t} \tag{2.56}$$

where v_0 (z) is the planar stationary solution given by (2.49)-(2.52) and v_{11} (x, z, t, e) is the small harmonic deformation imposed on the planar front (to first order in ε).

We now substitute the vectors of (2.55) and (2.56) into the governing equations (2.39)-(2.48), except using equation (2.46a) instead of (2.46) because latent heat is neglected. Expanding the equations of interface conditions (2.43), (2.44), (2.45), (2.46a) and (2.47) in a Taylor series at $z_0 = \varepsilon\zeta = 0$ and omitting all terms of $O(\varepsilon^2)$ and higher, we obtain the following equations for v_{11} upon cancellation of the common factor of $\varepsilon Cos(qx)e^{a_0 t}$:

For $z>0$:

$$\left(\frac{d^2}{dz^2} - q^2 + \frac{d}{dz} - a_0\right) c_{11}(z) = 0 \tag{2.57}$$

$$\left(\frac{d^2}{dz^2} - q^2\right) T_{11}(z) = 0 \tag{2.58}$$

For $z<0$:

$$\left(\eta\frac{d^2}{dz^2} - \eta q^2 + \frac{d}{dz} - a_0\right) c'_{11}(z) = 0 \tag{2.59}$$

$$\left(\frac{d^2}{dz^2} - q^2\right) T'_{11}(z) = 0 \tag{2.60}$$

The interface conditions (about $z = \varepsilon\zeta = 0$):

$$T_{11}(0) - T_{11}(0) + \zeta_{11} G\frac{n-1}{n} = 0 \tag{2.61}$$

$$c'_{11}(0) = k(k-1) + k\, c_{11}(0) \tag{2.62}$$

$$\frac{dc_{11}(0)}{dz} - \eta\frac{dc'_{11}}{dz} - (k-1)\, c_{11}(0) + (1-k)\,(k + a_0)\, \zeta_{11} = 0 \tag{2.63}$$

$$n\frac{dT_{11}^{'}}{dz}-\frac{dT11}{dz}=0 \qquad (2.64)$$

$$T_{11}(0) - Mc_{11}(0) + \zeta_{11}[G + q^2\gamma - M(k-1)] = 0 \qquad (2.65)$$

and the boundary conditions are:

$$c_{11}(\infty) = c_{11}^{'}(\infty) = 0$$

$$T_{11}(z_1) = T_{11}^{'}(z_2) = 0 \qquad (2.66)$$

A general solution for the vector $v_{11}(x,z,t;e) = (c_{11}, T_{11}, c_{11}^{'}, T_{11}^{'}, \zeta_{11})$ subject to the boundary conditions (2.66) is then given by:

$$c_{11}(z) = A_{11}\exp[-m_{11}z] \qquad (2.67)$$

$$T_{11}(z) = B_{11}\exp(-qz) \qquad (2.68)$$

$$c_{11}^{'}(z) = A_{11}^{'}\exp[m_{11}^{'}z] \qquad (2.69)$$

$$T_{11}^{'} = B_{11}^{'}\exp(qz) \qquad (2.70)$$

$$\zeta_{11} = D_{11} \qquad (2.71)$$

where A_{11}, B_{11}, A_{11}', B_{11}' and D_{11} are constants, m_{11} and m_{11}' are recovered by substituting equations (2.67) and (2.69) into equations (2.57) and (2.59) respectively, and

$$m_{11} = \frac{1}{2} + \sqrt{\frac{1}{4} + q^2 + a_0} \qquad (2.72)$$

$$m_{11}' = -\frac{1}{2\eta} + \frac{1}{\eta}\sqrt{\frac{1}{4} + \eta^2 q^2 + \eta a_0} \qquad (2.73)$$

Note that in writing equations (2.68) and (2.70) and the boundary conditions (2.66) we assume the system is infinite along x; thus we only consider deformations with wavelengths much smaller than the dimensions of the sample, i.e. $qz_{1,2} \gg 1$.

Applying equations (2.67)-(2.71) to the interface conditions (2.61)-(2.65), after some algebra, we have five linear homogeneous equations for five unknowns A_l, B_l, A_l', B_l' and D_l:

$$B_l - B_l' + D_l G \frac{n-1}{n} = 0 \tag{2.74}$$

$$kA_l - A_l' + k(k-1) D_l = 0 \tag{2.75}$$

$$(m + k - 1) A_l + \eta m' A_l' + (k-1)(k + a_0) D_l = 0 \tag{2.76}$$

$$B_l + n B_l' = 0 \tag{2.77}$$

$$M A_l - B_l + [M(k-1) - G - q^2 \gamma] D_l = 0 \tag{2.78}$$

For a non-trivial solution to exist, the determinant of the coefficients must vanish. Therefor, after some algebra, we find the dispersion relation reassembled in the scaled dimensionless form (see also equation 2.35):

$$\Delta(a_0, q) = a_0 + k\,[1 + \eta\, m'(a_0, q)] - (\tau - \beta q^2)\,[m_{11} - 1 + k\,(1 + \eta m_{11}')] = 0 \tag{2.79}$$

where

$$\beta = \frac{\gamma}{M(k-1)}, \qquad \tau = 1 - \frac{2G}{(n+1)(k-1)M} \tag{2.80}$$

As mentioned in section 2.3, to determine stability we must know the sign of Re(a_0). One can prove the so-called principle of exchange stabilities for this problem [12,13], i.e., one can show that in equation (2.79), $Re(a_0) = 0$ implies $Im(a_0) = 0$. The existence of an exchange stabilities means that we can set $a_0 = 0$ in equation (2.79) in order to investigate neutral stability. So, when looking for the threshold of instability, we can simply set $a_0 = 0$ in equation (2.79), and the condition of neutral stability then reads:

$$\Delta(0,\, q_c) = k\,[1 + \eta\, m'(0,\, q_c)] - (\tau_C - \beta\, q_C^2)\,[m(0,\, q_c) - 1 + k\,(1 + \eta m'(0,\, q_c)]=0$$

Or equivalently

$$\tau_C = \beta\, q_C^2 + \frac{k(1+\eta m_{11}'(0,q_C))}{m-1+k(1+\eta m_{11}'(0,q_C))} \qquad (2.81)$$

Just as discussed in section 2.3 we can also drawn the results of linear stability analysis here as well. Detailed discussions can be found in references 12 and 13. The absolute minimum τ_C at q_C (critical wavenumber associated with the most unstable mode) is such that

$$\left.\frac{d^2\tau}{dq^2}\right|_{q=q_C} = 0,$$

i.e.

$$\beta = \frac{k}{(m_{11}-1+k(1+\eta m_{11}'))^2}\left[\frac{1+\eta m_{11}'}{2m_{11}-1} - \frac{\eta^2 m_{11}-1}{2\eta m_{11}'+1}\right] \qquad (2.82)$$

Combining equations (2.81) and (2.82) and eliminating q_C, in the limit of small β so that we can omit $\sim\beta$ terms as compared to $\sim\beta^{1/3}$ terms, we obtain

$$G_C(\beta)\xrightarrow{\beta\to 0}\frac{(n+1)(k-1)M}{2}\cdot\left\{\frac{1}{1+\eta k} - 3\left[\frac{k(1+\eta)}{4(1+\eta k)^2}\right]^{2/3}\beta^{1/3}\right\} \qquad (2.83)$$

Figure 18 shows G_C, the dimensionless combination of temperature and concentration, against β, a dimensionless quantity which is proportional to the velocity in the case of $\eta = 0$. It is equivalent to Figure 13 ($\underline{G}$ vs $\underline{V}$) as

$$G = \frac{GD}{VT_M} \quad \text{and} \quad \beta = \frac{\gamma}{M(k-1)} = \frac{d_0/(D/V)}{M(k-1)}$$

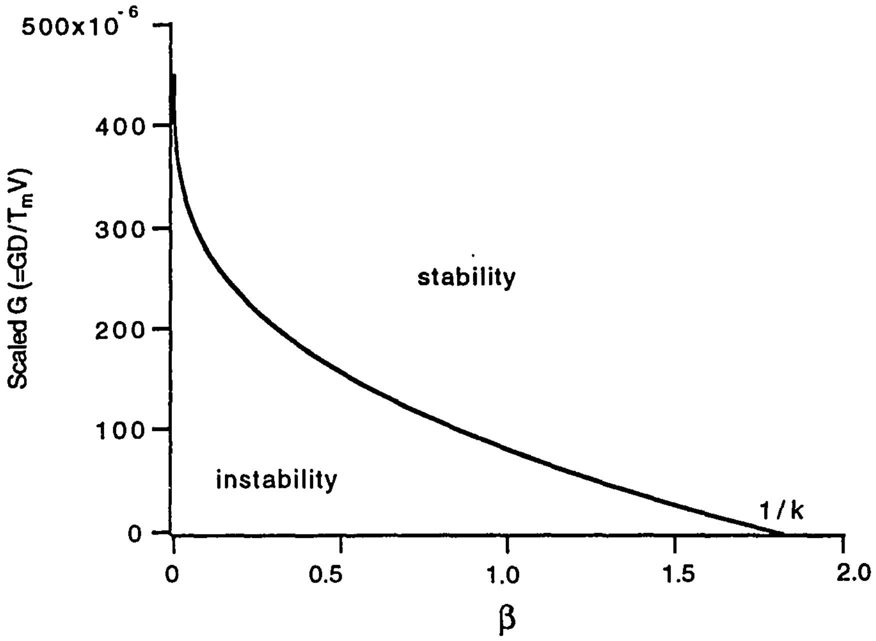

Figure 18 G_C , the dimensionless combinations of temperature gradient and concentration, against β, a dimensionless quantity which is proportional to V in the case of $\eta = 0$. (SCN/Acetone, c=0.1 wt%)

On the G-β plot we have stability for $G > G_C$ and instability for $G < G_C$. G_C represents the marginal stability curve. Note that for $\beta \geq \frac{1}{k}$, $G_C = 0$ and we have stability for any $G > 0$. Thus for $\beta \geq \beta_{max}$ we have what metallurgists call absolute stability. The associated absolute restabilization velocity, equation (2.37), is then derived from

$$\frac{1}{k} = \beta_{max} = \frac{d_0/(D/V_{max})}{M(k-1)},$$

So

$$V_{max} = \frac{Dmc_\infty(1-k)}{d_0 T_M k}. \tag{2.84}$$

2.4.3.2 The Nonlinear Expansion

Having examined the stability of the planar interface to infinitesimal disturbances, we now investigate the stability of the planar interface solution to finite amplitude disturbances. Owing to the inherent nonlinearities, the superposition principle as used in the linear stability analysis no longer applies, and a non-linear iteration (higher order harmonics of the fundamental disturbances) must come into play.

Generalizing equation (2.55), we now consider solutions to the governing equations of the form

$$v\,(z,x,t;\,\varepsilon) = \sum_{n=0}^{\infty} \varepsilon^{n} A^{n}(t) v_{n}\,(x,z,t) \tag{2.85}$$

where $v\,(z,x,t;\,\varepsilon) = (c,\,T,\,c',\,T,\,\varepsilon\zeta)$, a general vector.

We assume that

$$v_{11}\,(z,x,t;\varepsilon) = A(t)\ Cos(qx)\ v_{11}(z) \tag{2.86}$$

where $A(t)$ is an unknown amplitude. To this lowest order, the interface satisfies the asymptotic expression

$$z \sim \zeta_{11}(x,t) = A(t)\ Cos(qx) \tag{2.87}$$

In general, the interface equation is

$$z(x,t) = A(t)\ Cos(qx) + A^{2}(t)\ \zeta^{2}(x) + A^{3}(t)\ \zeta^{3}(x) + O(A^{4}) \tag{2.88}$$

Assumptions (2.86) and (2.87) only enable us to study periodic solutions with a single wave number q and its harmonics being generated by higher orders in ε. This is not too drastic a restriction: on the one hand, observed experimental structures are essentially periodic; on the other hand, close to the bifurcation only a narrow band of wave numbers are linearly unstable while their harmonics are stable.

The forms of $\zeta_2(x)$ and $\zeta_3(x)$ can be motivated as follows:[65] starting from equation (2.87), upon comparing the forms of

$$\zeta_1^2(x,\, t) = \frac{1}{2}\, A^2(t)\, [1 + Cos(2qx)]$$

and

$$\zeta_1^3(x,\, t) = \frac{1}{4} A^3(t)\, [3\, Cos(qx) + Cos(3qx)]$$

with the second and the third terms of (2.88), respectively, it becomes obvious that we should choose

$$\begin{aligned} v\,(z,x,t;\, \varepsilon) = {} & \sum_{n=0}^{\infty} \varepsilon^n\, A^n(t) v_n(x,z,t) \\ & = v_0(z) + \varepsilon A(t)\, V_{11}(z)\, Cos(qx) + \varepsilon^2 A^2(t) [V_{20}(z) + V_{22}(z)\, Cos(2qx)] \\ & \quad + \varepsilon^3 A^3(t)\, [V_{31}(z)\, Cos(qx) + V_{33}(z)\, Cos(3qx)] \\ & \quad + \sum_{n=4}^{\infty} \varepsilon^n\, A^n(t) v_n\, (x,z,t) \end{aligned} \tag{2.89}$$

where v_{ij} (z) are the coefficients of a term in (2.89) of the form $A^i(t)\, Cos(jqx)$ with $v_{00}(z) = v_0$, $v_{11}(z)$ has been solved in section 2.4.3.1. Or, more explicitly write all the quantities to the 3rd order:

$$\begin{bmatrix} c(x,z,t;\varepsilon) \\ c'(x,z,t;\varepsilon) \\ T(x,z,t;\varepsilon) \\ T'(x,z,t;\varepsilon) \\ \varepsilon\zeta(x,t;\varepsilon) \end{bmatrix} = \begin{bmatrix} c_0(z) \\ c_0'(z) \\ T_0(z) \\ T_0'(z) \\ 0 \end{bmatrix} + \varepsilon A(t) \begin{bmatrix} c_{11}(z) \\ c_{11}'(z) \\ T_{11}(z) \\ T_{11}'(z) \\ \zeta_{11} \end{bmatrix} Cos(qx)$$

$$+\ \varepsilon^2 A^2(t)\begin{bmatrix} c_{20}(z)+c_{22}(z)Cos(2qx) \\ c_{20}'(z)+c_{22}'(z)Cos(2qx) \\ T_{20}(z)+T_{22}(z)Cos(2qx) \\ T_{20}'(z)+T_{22}'(z)Cos(2qx) \\ \zeta_{20}+\zeta_{22}Cos(2qx) \end{bmatrix}$$

$$+\ \varepsilon^3 A^3(t)\begin{bmatrix} c_{31}(z)Cos(qx)+c_{33}(z)Cos(3qx) \\ c_{31}'(z)Cos(qx)+c_{33}'(z)Cos(3qx) \\ T_{31}(z)Cos(qx)+T_{33}(z)Cos(3qx) \\ T_{31}'(z)Cos(qx)+T_{33}'(z)Cos(3qx) \\ \zeta_{30}Cos(qx)+\zeta_{33}Cos(3qx) \end{bmatrix} \qquad (2.90)$$

We next examine equation (2.89) for terms proportional to *Cos(qx)* and find them to contain the amplitude functions $A(t)$ and $A^3(t)$. Hence we conclude that $A(t)$ satisfies the following amplitude equation[66] :

$$\frac{dA}{dt} = a_0 A(t) - \varepsilon^2 a_1 A^3(t) + \sum_{n=2}^{\infty} a_n \varepsilon^{2n} A^{2n+1}(t) \qquad (2.91)$$

Now we substitute (2.90) and (2.91) into the governing equations (2.39)-(2.48). Recall the planar stationary solution of $v_0(z)$ of equations (2.49)-(2.52), and the interface and boundary conditions expanded in a Taylor series about $z = \varepsilon\zeta(x,t) = 0$, we then obtain (after some tedious computation) a set of differential equations of $v = (c,\ T,\ c',\ T',\ \varepsilon\zeta)$ for each ε^n; $n = 1,\ 2,\ 3,\ \cdots$. Defining an operator $D_z = \frac{d}{dz}$, we can write the differential equations for the various orders of ε.

The system for $n = 0$ is satisfied identically since $v_0(z)$ is the exact planar interface solutions (see equations (2.49)-(2.52)).

For $O(\varepsilon)$, which corresponds to $i = j = 1$, there results one set of equations which is proportional to $A(t)Cos(qx)$. It is identical to the results of linear stability analysis in section 2.4.3.1.

2.4.3.3 The $O(\varepsilon^2)$Problem

For $O(\varepsilon^2)$ there are two sets of equations: one proportional to $A^2(t)$ and the other to $A^2(t)Cos(2qx)$. The differential equations for each case are:

$$\begin{cases} (D_z^2 + D_z - 2a_0)c_{20} = 0 \\ D_z^2 T_{20} = 0 \\ (\eta D_z^2 + D_z - 2a_0)c_{20}' = 0 \\ D_z^2 T_{20}' = 0 \\ D_z \zeta_{20} = 0 \end{cases} \tag{2.92}$$

and

$$\begin{cases} (D_z^2 + D_z - 2a_0 - 4q^2)c_{22} = 0 \\ D_z^2 T_{22} = 0 \\ (\eta D_z^2 + D_z - 2a_0 - 4q^2)c_{22}' = 0 \\ D_z^2 T_{22}' = 0 \\ D_z \zeta_{22} = 0 \end{cases} \tag{2.93}$$

The boundary conditions (2.48) implies

$$c_{20}(c_{20}') \xrightarrow{z \to \pm\infty} 0, \qquad T_{20}(T_{20}') \xrightarrow{z \to z_1(z_2)} 0$$

Equations (2.92) should posses solutions of the form:

$$\begin{cases} c_{20}(z) = A_{20}e^{-m_{20}z} \\ T_{20}(z) = B_{20}(1-\dfrac{z}{z_1}) \\ c'_{20}(z) = A'_{20}e^{-m'_{20}z} \\ T'_{20}(z) = B'_{20}(1-\dfrac{z}{z_2}) \\ \zeta_{20} = D_{20} \end{cases} \tag{2.94}$$

where the five constants A_{20}, B_{20}, A_{20}', B_{20}' and D_{20} can be obtained by using the interface conditions (2.42)-(2.47). m_{20} and m'_{20} are given by:

$$\begin{cases} m_{20} = m(2a_0,0) = \tfrac{1}{2} + \sqrt{\tfrac{1}{4} + 2a_0} \\ m'_{20} = m'(2a_0,0) = -\tfrac{1}{2\eta} + \tfrac{1}{\eta}\sqrt{\tfrac{1}{4} + 2\eta a_0} \end{cases} \tag{2.95}$$

Let us point out again that we are using a finite sized thermal box [12] (boundary condition (2.48)). If we neglect the thermal size of the box and impose $T_{20}(T'_{20}) \xrightarrow{z\to\pm\infty} 0$ as was assumed by Wollkind and Segel [13], B_{20} and B_{20}' will be zero. In fact [12], only for η = 0 (such as directional solidification in plastic crystals) does one recover $B_{20} = B_{20}' = 0$, in which limit the thermal boundary conditions are irrelevant [67].

Almost identically, we can solve for v_{22}:

$$\begin{cases} c_{22}(z) = A_{22}e^{-m_{22}z} \\ T_{22}(z) = B_{22}e^{-2qz} \\ c'_{22}(z) = A'_{22}e^{m'_{22}z} \\ T'_{22}(z) = B'_{22}e^{2qz} \\ \zeta_{22} = D\zeta_{22} \end{cases} \tag{2.96}$$

where A_{22}, B_{22}, A_{22}', B_{22}' and D_{22} are constants and

$$\begin{cases} m_{22} = m(2a_0, 2q) = \frac{1}{2} + \sqrt{\frac{1}{4} + 2a_0 + 4q^2} \\ m'_{22} = m'(2a_0, 2q) = -\frac{1}{2\eta} + \frac{1}{\eta}\sqrt{\frac{1}{4} + 2\eta a_0 + 4\eta^2 q^2} \end{cases} \qquad (2.97)$$

Finally, let us consider the so-called mean motion terms at order ε^2. The mean terms of $v(x,z,t;\varepsilon)$ is given by

$$\lim_{L\to\infty} \frac{1}{2L} \int_{-L}^{L} v(x,z,t;\varepsilon)dx = v_0(z) + \varepsilon^2 v_{20}(x) + O(\varepsilon^4) \qquad (2.98)$$

Thus the quantity $\varepsilon^2 A^2(t) v_{20}(z)$ represents the alteration of the mean of the solution due to the type of perturbation introduced in section 2.4.3.2. The mean position of the interface is now at

$$z = 0 + \varepsilon^2 A^2(t)\, D_{20} = \varepsilon^2 A^2(t) \frac{q(1-n)}{2(1+n)} \qquad (2.99)$$

Since $n = \frac{K_{th}(solid)}{K_{th}(liquid)} > 1$, the quantity on the right of (2.99) is negative. Thus one nonlinear effect is that the mean position of the interface lags behind its position of $z=0$ as determined by the linear theory.

2.4.3.4 The $O(\varepsilon^3)$ Problem -- Calculation of a_1 .

In order to calculate the coefficient a_1 of the cubic term in the amplitude equation, we only need to consider, among the $O(\varepsilon^3)$ contributions, the term v_{31}., i.e. $i=3, j=1$ with terms are proportional to $A^3(t)\, Cos(qx)$. The resulted differential equations are:

$$\begin{cases} (D_z^2 - q^2 + D_z - 3a_0)c_{31}(z) + a_1 c_{11}(z) = 0 \\ (D_z^2 - q^2)T_{31}(z) = 0 \\ (\eta D_z^2 - \eta q^2 + D_z - 3\dot{a}_0)c'_{31}(z) + a_1 c'_{11}(z) = 0 \\ (D_z^2 - q^2)T'_{31}(z) = 0 \end{cases} \qquad (2.100)$$

the general solutions for (2.100) subject to the boundary condition (2.48) are:

$$\begin{cases} c_{31}(z) = A_{31}e^{-m_{31}z} + \dfrac{a_1}{2a_0}A_{11}e^{-m_{11}z} \\ T_{31}(z) = B_{31}e^{-qz} \\ c'_{31}(z) = A'_{31}e^{m'_{31}z} + \dfrac{a_1}{2a_0}A'_{11}e^{m'_{11}z} \\ T'_{31}(z) = B'_{31}e^{qz} \end{cases} \tag{2.101}$$

where A_{31}, B_{31}, $A_{31}{}'$, $B_{31}{}'$ are constants to be determined and

$$\begin{cases} m_{31} = m(3a_0, q) = \tfrac{1}{2} + \sqrt{\tfrac{1}{4} + 3a_0 + q^2} \\ m'_{31} = m'(3a_0, q) = -\tfrac{1}{2\eta} + \tfrac{1}{\eta}\sqrt{\tfrac{1}{4} + 3\eta a_0 + \eta^2 q^2} \end{cases} \tag{2.102}$$

Now substitute v, containing v_0, v_{11}, v_{20}, v_{22} and v_{31} into the interface conditions (2.43), (2.44), (2.45), (2.46a) and (2.47); we get five linear equations for five unknowns A_{31}, B_{31}, $A_{31}{}'$, $B_{31}{}'$ and ζ_{31}:

$$\begin{cases} B_{31} - B'_{31} + G(1 - \tfrac{1}{n})\zeta_{31} = d_4 \\ k(A_{31} + \dfrac{a_1}{2a_0}A_{11}) - (A'_{31} + \dfrac{a_1}{2a_0}A'_{11}) + k(k-1)\zeta_{31} = d_5 \\ -A_{31}m_{31} - \dfrac{a_1}{2a_0}A_{11}m_{11} - (k-1)(A_{31} + \dfrac{a_1}{2a_0}A_{11}) \\ \qquad -\eta(A'_{31}m'_{31} + \dfrac{a_1}{2a_0}A'_{11}m'_{11}) - (k-1)(k+3a_0)\zeta_{31} \\ \qquad +(k-1)a_1 = d_3 + a_0 d_0 \\ B_{31} + nB'_{31} = d_2 \\ -M(A_{31} + \dfrac{a_1}{2a_0}A_{11}) + [G + \gamma q^2 - M(k-1)]\zeta_{31} + B_{31} = d_1 \end{cases} \tag{2.103}$$

where the constants d_0, d_1, d_2, d_3, d_4 and d_5 are expressions in terms of the amplitude coefficients of v_0, v_{11}, v_{20}, v_{22} (i.e. A_0, A_{11}, B_{11}, etc.) [68]. They are listed (for $a_0 = 0$) in reference 12.

The associated determinant is easily checked to be $\Delta(3a_0, q)$ -- where $\Delta(a_0, q)$, given by equation (2.81), is the corresponding quantity for the linear problem. So, at the bifurcation, the determinant vanishes exactly, and equations (2.103) are degenerate. One must therefore impose a condition of compatibility among equations (2.103) for $a_0 = 0$, which determines the coefficient a_1. Eliminating A_{31}, B_{31}, A_{31}', B_{31}', ζ_{31} and taking the limit of $a_0=0$, we get [12, 65]:

$$a_1 = \frac{S}{F(k-1)} \tag{2.104}$$

where

$$\begin{cases} S = d_3 - \eta m_{01}' d_5 - \dfrac{m_{01} - 1 + k(1 + \eta m_{01}')}{M}\left(d_1 - \dfrac{d_2 + m d_4}{1+n}\right) \\ F = 1 - \dfrac{\tau - \beta q^2}{2m_{11} - 1} + \eta k \cdot \dfrac{1 - \tau + \beta q^2}{2\eta m_{11}' + 1} \end{cases} \tag{2.105}$$

We have derived a_1 for the general case $n \neq 1 \neq 0$, $\eta \neq 1$. If we let $n=\eta=1$ (symmetric model), we recover the results of Langer and Turski [14]; if simply let $\eta=0$ (one sided model), we recover Wollkind and Segel's analysis [13, 65]. Directional solidification in plastic crystals can be categorized in $\eta=0$ since $D'/D \sim 10^{-5}$. In such a case, $a_1 = \dfrac{S_{31}(0)}{F_0(k-1)} = a_1(q_c, \beta, G, V, c)$.

As discussed in section 2.4.1, the sign of a_1 gives a qualitative prediction about the nature of the bifurcation. The practical exploitation of a_1 involves two steps: one first solves the neutral stability equations (2.81), (2.82) and (2.83) and finds the critical wave number $q_c(\beta)$ and the temperature gradient $G(\beta)$. One then inserts these quantities into equation (2.104) to obtain the value of a_1.

It is possible, however, from the small-β (i.e. small velocity) expansion of equation (2.81), (2.82), (2.83), to calculate the small velocity expansion of a_1. In fact, from (2.81) with $\eta=0$, one can obtain $q_c = q_c(\beta)$. Then substitute $q_c = q_c(\beta)$ into a_1 to eliminate q_c. In the limit $\beta \to 0$, $n \approx 1$ (i.e. using highly conducting plates), one finally gets, valid only very close to the $\underline{G}$-β plane:

$$\begin{aligned} a_1 &\propto \frac{n-1}{n+1}\cdot\frac{1}{8\beta}+\left(\frac{4k}{\beta}\right)^{2/3}\left(\frac{k^2+4k-2}{4k}\right) \\ &\to \frac{k^2+4k-2}{4k} \end{aligned} \tag{2.106}$$

which is the result first found by Caroli, et al [12]. Thus when latent is neglected, the sign of a_1 is determined uniquely by k.

2.4.4 The Weakly Nonlinear Stability Analysis Including Latent Heat -- Calculation of a_1.

In the previous nonlinear stability analysis the latent heat of fusion L, which appears explicitly in the equation describing the local balance of energy across the solid-liquid interface - equation (2.46), was neglected. Alexander et al found [24] that allowing for a finite latent heat results in positive values of the Landau coefficient a_1, and hence two-dimensional bands of small stable amplitude, for a much enhanced range of growth conditions, especially at low solute concentrations. Using the same perturbative approach in section 2.4.4, with latent heat included but with $\eta = 0$, the Landau coefficient a_1 is given by [24, 26] (Note that there are some typographical errors in the a_l expressions in reference 24 and 26.)

$$\begin{aligned}
\mathrm{Re}(a_1) = \{ & \frac{k(k-1)}{16} - k(k-1)(\zeta_{11} + \frac{1}{2}\zeta_{20}) - kA_{11} \\
& + A_{10}(2q^2\zeta_{20} - \frac{1}{4}q^2 m_{10}) + q^2 A_{20} \\
& - \frac{m_{20}A_{20}}{2}(m_{20} + k - 1) + (m_{10} + k - 1) \\
& [A_{11} - (1-k)\zeta_{11} + \frac{m_{20}A_{20}}{2} - \frac{1-k}{2}\zeta_{20} \\
& \frac{k-1}{16} - \frac{3q^2(k-1)A}{16k} - \frac{4\zeta_{20}qB_{10}}{n+1}]\} \\
& [\frac{k-1}{2} + \frac{A_{10}}{2m_{10}-1} + \frac{(k-1)(m_{10}+k-1)}{2Iq}]^{-1}
\end{aligned} \tag{2.107}$$

where A_{ij}, B_{ij} and ζ_{ij} are given in Appendix A, and

$$I^{-1} = \frac{kDL}{(k-1)(1+n)K_{th}mc_\infty} \tag{2.108}$$

is a latent heat parameter, and

$$A = \frac{\sigma T_M V k^2}{mLDc_\infty(k-1)} \tag{2.109}$$

is a scaled surface energy.

As pointed out by Merchant and Davis [25, 26], by including latent heat in the analysis, the critical velocity for SCN-acetone system is shifted significantly compared to that for L=0, bringing regions of supercritical bifurcation into an experimentally accessible parameter range. For a qualitative analysis, let's examine a modified form of a_l [25] valid in the low pulling speed limit:

$$a_l \sim \frac{1-n+I^{-1}(1+n)}{(1+n)(1+I^{-1})A/k} + O(\frac{k}{A^{2/3}}) \\ \sim \frac{k}{(1+I)A} - \frac{(n-1)k}{(n+1)(1+I^{-1})A} \tag{2.110}$$

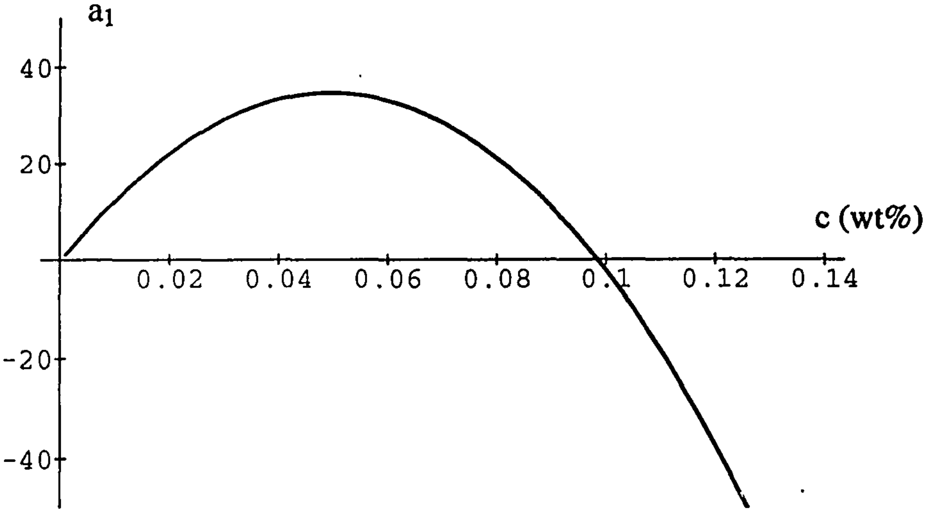

Figure 19 a_l vs c based on the simplified a_l expression (2.110). (SCN/C152, G=52K/cm)

As noted by Merchant and Davis , if (1-n) is far from zero, latent heat effects are not very important. However, if $n \approx 1$, as in plastic crystals, the magnitude, and indeed the sign of a_l is very sensitive to latent-heat effect. As a result, the impurity concentration of the solute c_∞, becomes crucial in determining the sign of a_l. With decreasing c_∞, the

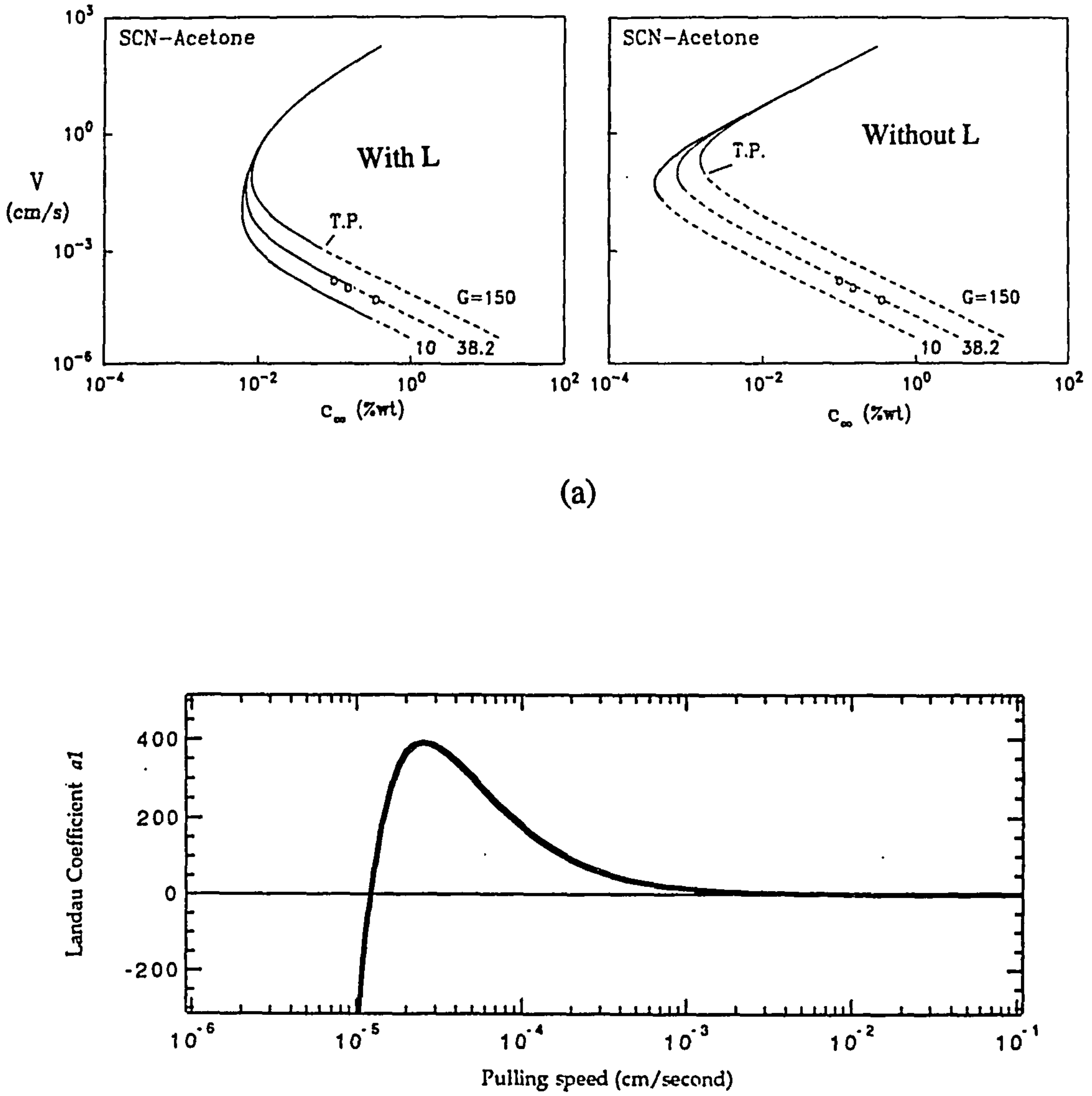

(a)

(b)

Figure 20 (a) Marginal stability curve of SCN/Acetone with and without latent heat. Subcritical region is indicated by dashed line (Reproduced from reference 25). (b) a_l against V from the full a_1 expression of (2.107). As the critical velocity increases, a_l changes sign from negative to positive.(SCN/Acetone, G=38.2 K/cm) thermal field becomes increasingly important; a_l should change sign from negative to positive at a crossover concentration c_t, where the subcritical bifurcation for $c>c_t$ will change into a supercritical bifurcation for $c<c_t$. This is depicted in Figure 19. In Figure 20 we utilized the full a_1 expression (equation 2.107) to calculate the crossover point at which a_1 changes sign. The crossover point is shifted significantly as the latent heat is included (a); and as the solute concentration is reduced, the critical pulling speed increases, as a result a_1 changes sign from negative to positive, converting the bifurcations from subcritical to supercritical (b).

One of the main topics of this dissertation is to prove experimentally the existence of this bifurcation crossover in plastic crystal systems during directional solidification. Similar effects have been found in the Couette-Taylor hydrodynamic instability.[69]

2.4.5 Hysterisis

One convenient way to categorize a bifurcation as either subcritical or supercritical is to examine its velocity hysteresis (see Figure 15). The maximum possible hysteresis $\Delta V_{amx}=V_C^+ - V_C^-$, set by the limits of stability of the planar and cellular interfaces, is given by

$$\Delta V_{\max} = \begin{cases} \dfrac{a_1^2}{4a_2 s}, & a_1 < 0 \\ 0, & a_1 > 0 \end{cases} \qquad (2.111)$$

where s is the slope of $a_0(V)$ at $V=V_C$. Detailed derivation is shown in Appendix A.

3. Experimental Methods

Considerable effort was devoted to the design of the experimental setup and to the preparation of samples which are both crucial to the success of the experiments. In this chapter, I will first present the design and construction of our directional solidification apparatus, and will subsequently describe the sample preparation procedures in section 3.2.

3.1 Design and Construction of the Experimental Apparatus

To study the instability of a planar crystal-melt interface and the planar-cellular bifurcation, two key experimental factors must be satisfied: (i) a precise linear motion and a steep and stable temperature gradient are required, (ii) a pure plastic crystal (in our case Succinonitrile) mixed with an accurately known amount of impurity (in our case Coumarin 152) at low concentrations (less that 0.5 wt%) must be prepared. Since the critical velocity for the bifurcation in this system is of order 1 μm/s, and the crossover of the subcritical to supercritical transition occurs as the concentration decreases, very small deviations from pulling speed linearity or stability, or uncontrolled impurity concentrations can cause significant variations and mask the phenomena under study. To study the dynamic process of the planar-cellular instability, a laser fiber coupling mechanism (to generate local heat perturbation to the interface) is integrated into the apparatus.

We have designed and constructed a precision directional solidification apparatus based on the principle of

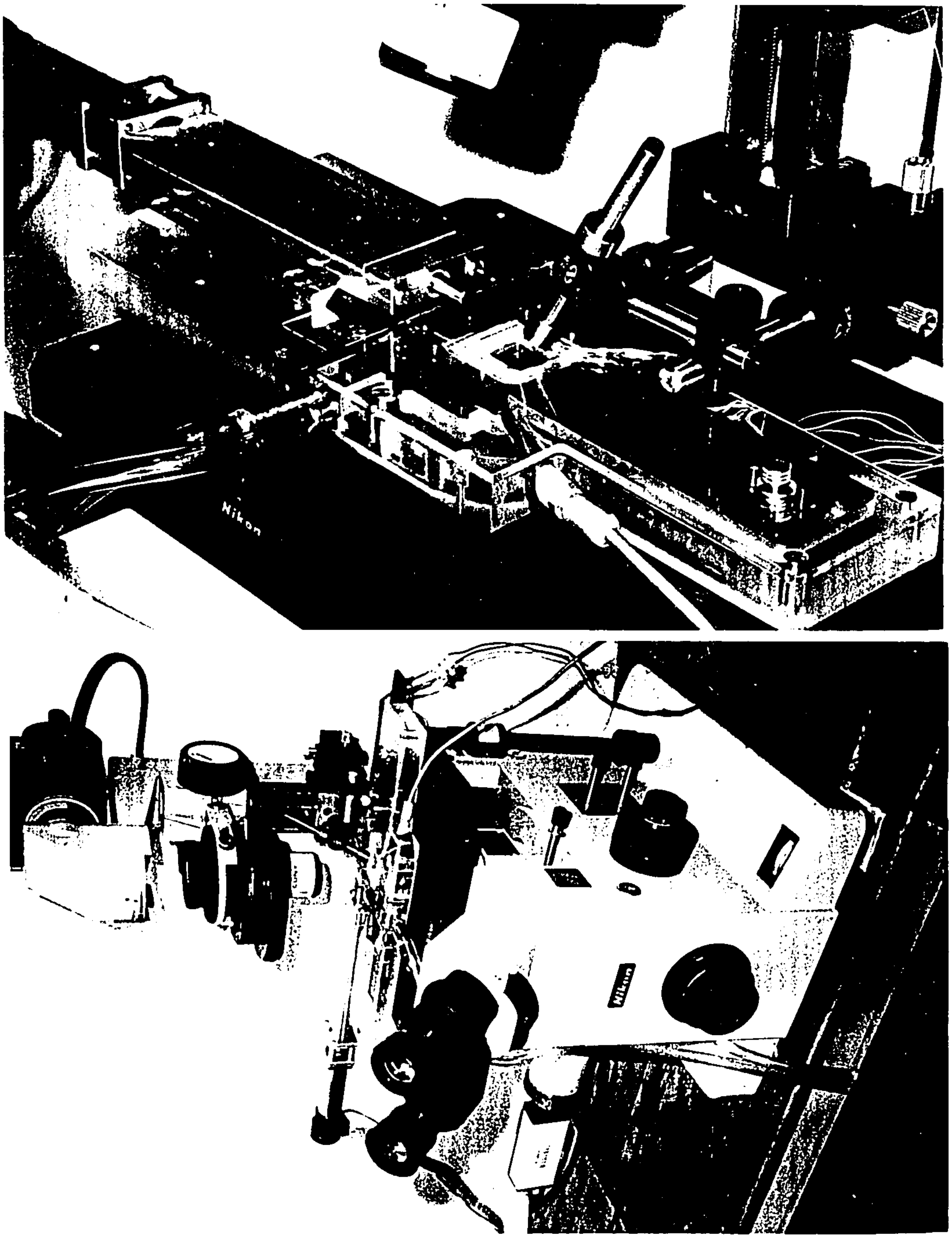

Figure 21 Directional solidification apparatus. Growth chamber with fiber optic (top). Mounted on Nikon Diaphot microscope (bottom).

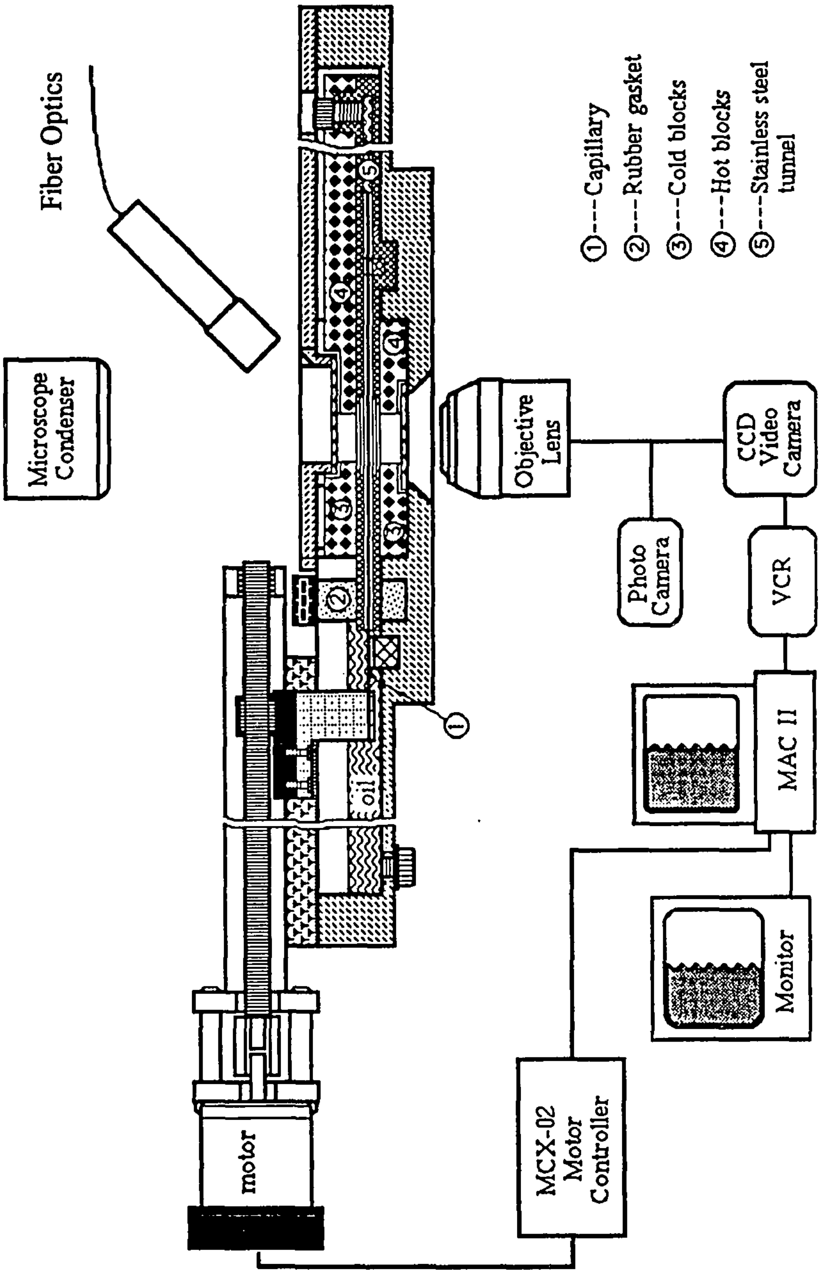

Figure 22 Cross-sectional view of whole apparatus assembly. The crystal growth chamber section is shown at 75% of actual size.

the directional solidification stage of Jackson and coworkers [70, 71], but significant improvements have been incorporated into our setup. The apparatus consists of a computer-controlled motorized translation stage to pull the sample capillary through the temperature gradient, and crystal growth chamber to provide the temperature gradient, all contained in a Lucite case that provides thermal isolation, and a laser-fiber coupling system to provide local laser perturbation to the sample. The apparatus is mounted on the stage of a Nikon Diaphot microscope. (see Figure 21 and Figure 22).

3.1.1 Crystal Growth Chamber

The crystal growth chamber is the central part of the apparatus. The design strategy involves maintaining highly stable temperature control capability and thermal isolation of each part, submerging the sample cell in oil to provide optical index matching and thermal contact, and miniaturizing the apparatus because it affects the microscope platform and focal distance. Previous experiments in our laboratory have employed thin glass capillaries (Manufactured by Vitro Dynamics[72]) as sample cells. This not only provides a way of avoiding sample contamination during preparation (which we will discuss in the next section), but it also greatly reduced the size of the conventional directional solidification setup. The central part of the crystal growth chamber is a rectangular stainless steel tunnel with sapphire windows. This tunnel is sandwiched between copper cold and hot blocks whose temperatures are controlled by a Lauda RMS 6 and a YSI-72 proportional temperature controller respectively to better then 0.01^0. Mineral oil is used to fill the tunnel for uniform thermal conduction and for optical matching. The top section of the hot block is elongated to keep the entire liquid side of the interface molten, maintaining an initial uniform dye concentration on the whole liquid side of the interface. The gap between the cold and hot blocks can be varied from 0.48 to 0.95cm for temperature gradients up to several hundred degrees per centimeter (typically 100 K/cm). The high thermoconductivity of stainless' steel and sapphire (both with similar values of thermoconductivity coefficient at ~10^{-2} cal/(cm K s)) ensures a very linear temperature field across the gap (Figure 23) (Refer section 3.2.4 for the procedures in measuring the temperature field.).

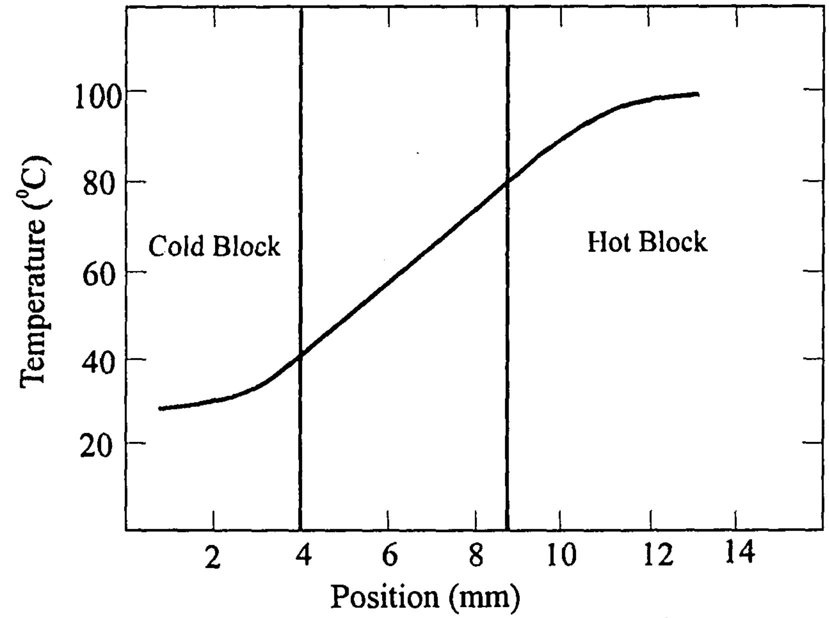

Figure 23 Temperature profile across the gap (typical). Determined by pulling a mini-thermistor repeatedly through the stainless steel tunnel.

Ideally, the real temperature gradient at the sample should be set by the temperatures of the hot and cold blocks and the distance between them, but as seen from Figure 23, it will obviously be smaller. Even with attention to the thermal contact (or thermal isolation) to particular parts on our apparatus, we still noticed experimentally, in the best case, about 20% difference. The major factor is due to the thermal contact between the cold/hot blocks and the stainless steel tunnel. Nevertheless, the temperature gradients always appear linear in the region between the cold and hot blocks.

Two mechanical guides are precisely located inside and outside the tunnel to ensure accurate orientation and linear motion of the sample capillary. A rubber gasket which was precisely machined after being dipped into liquid nitrogen served to contain the mineral oil in the oil reservoir on the left and inside the tunnel only.

3.1.2 Programmable Motor Driven Stage

The motion control system is a MicroMo[73] DC servo motor with a Hewlett Packard integral optical encoder (500 pulses per revolution) controlled by a MicroMo Unicontroller series MCX-02. The controller is interfaced to a Macintosh II computer (or a PC) through an RS232 serial interface which provides programmable (using Basic language) precision position and velocity control. The velocity increment can be programmed to be as small as required (typically 0.03 mm/s). The free traveling distance of the capillary is 72mm. We first used a Velmex Unislide[74] translation stage to convert the motion from rotational to translational. With this stage, the translational velocity of the capillary was initially found to be constant within ~1%. But as this stage lacks ball bearings and its sliding aluminum surfaces are subject to wear, this velocity deviation increased to about 2%. We then replaced it with a precision crossed roller bearing translation stage CTC-460 from MicroKinectics.[75] We then again conducted the pulling speed tests on this new stage. We used a C program (written by Wolfgang Losert and

Martin Muschol in this lab) to scan a mark (for example, a sharp vertical line perpendicular to the pulling direction on the capillary) to monitor its position against time. If the pulling speed is ideally uniform the position-time plot should be a perfect straight line. But with mechanical imperfections of the pulling stage, there will be some degree of variation from linearity. With the Velmax Unislide this test showed a typical oscillation of the position of 4 pixels, indicating a velocity fluctuation of about 2%. In contrast, with the new pulling stage from Micro Kinetics no noticeable deviation from linearity was detected within the experimental error of ±0.15 pixels.(see Figure 24)

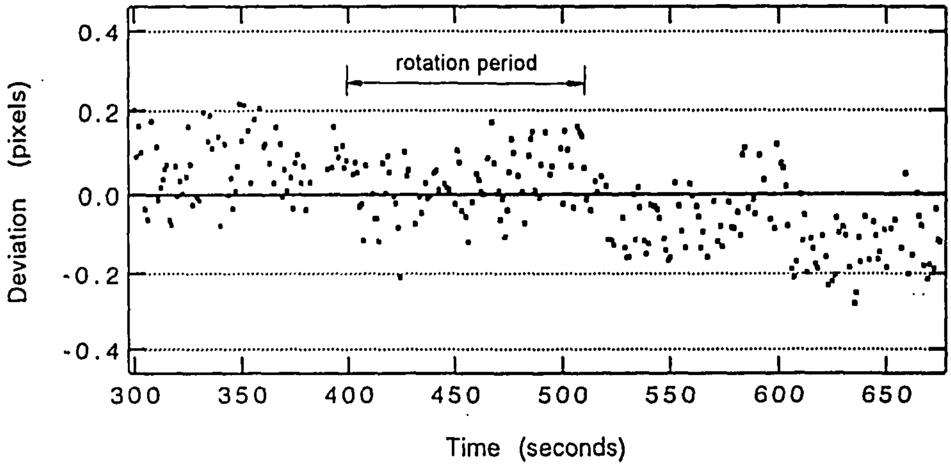

Figure 24 Velocity stability of the Micro Kinetics pulling stage (Model CTC-460). The pulling speed is at V=2.75 µm/s. 1 pixel = 3.1285 µm. (Interpolated position of the line minus local position with constant velocity.) One rotation of the screw is indicated by the arrow.

3.1.3 Laser-fiber Perturbation Apparatus

The laser perturbation system employs an Ar^{++} laser operated at 488nm (Spectra Physics 165) and a multi-mode optical fiber with a core diameter of 8.7 μm.[76] The output end of the fiber is equipped with a miniature converging lens and is mounted on a Newport[76] x-y-z micromanipulator. The perturbing laser spot at the sample interface has a diameter of about 10-30 μm. The typical power output from the fiber is 8-10 mW. An electro-mechanical shutter is placed between the laser and the laser-fiber coupler to control the duration of the perturbation on the sample.

3.2 Sample Preparation

3.2.1 Sample Purification and Sample Cell Preparation

The starting material, SCN (succinotitrile, $NC(CH_2)_2CN$, from Fluka, 99%), is vacuum distilled four times, with the first 20 and last 25% of each round rejected. A mechanical pump provides a vacuum of about 100-140 mtorr, resulting in a boiling temperature of the material of about 110 ^oC, at which the distillation is carried out. The purified SCN is finally transferred, again by vaccum distillation, to a cylindrical style addition funnel (see figure 25) for loading processes (section 3.2.2).

The sample cells are rectangular glass capillaries (from Vitro Dynamics). After many tests, we chose capillaries with an inside dimension of 100 x 2000 μm, roughly 30cm long. (There have been several discussions [18,23] about the effects of sample thickness and aspect ratio. We found the size we chose is appropriate in satisfying a near two-dimension model and eliminating transverse effects.) We cleaned the capillaries by funneling a hot 'liqui-nox' cleaning solution through them, followed by acetone and chromic acid and finally rinsing them extensively with distilled water. A flow vacuum helps to pull the fluids through the narrow capillaries. The cleaned capillaries were then put into a long glass tube and baked (at 200 ^{0}C) under vacuum over night, and finally they were flamed sealed at both ends for storage.

3.2.2 Loading the Materials into Sample Cells

The choice of the second component as the impurity was dictated by several criteria: it should be soluble in SCN at the desired concentrations (in our case $\leq 1\%$), both the melting and freezing points should be depressed linearly with the concentration of the impurity (the liquidus and solidus curves should be straight lines). Another requirement is that this two-component system should have an adequate partition coefficient k; k should be less than 0.45 but not too small because the critical velocity will be too small if k is very small; this second component should also absorb laser light to generate heat perturbations for our experiments. Finally the thermodynamic parameters, D, m, k, c, should be known or readily measurable. Coumarin 152 (C152, a yellow laser dye purchased from Sigma Chemical Co.) was selected as the second component. Its fluorescence provides a convenient means of determining the above thermodynamic parameters. It also absorbs the laser light to the level necessary to create a significant thermal perturbation (see section 4.2) and also facilitates obtaining a single well-oriented crystal (see section 4.1.1).

We first load a pure SCN sample immediately after the distillation in order to test the material for purity (procedures are described in the next paragraph). Upon finishing the purity test satisfactorily (see section 3.2.3), we then proceed as follows.

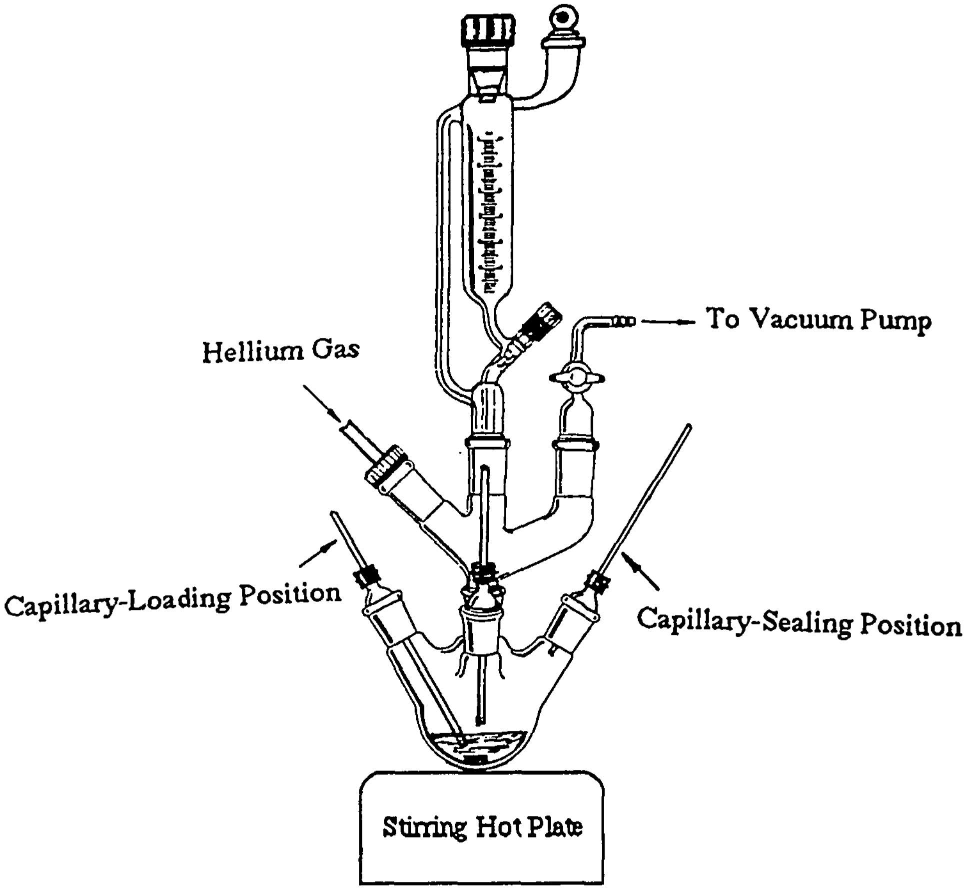

Figure 25 Schematic illustration of loading SCN/C152 into the capillaries.

To load the SCN/C152 samples, three capillaries were put into a multi-neck flask at the same time. The multi-neck flask is connected to the vacuum pump and to a helium gas cylinder (see Figure 25). A carefully weighed amount of C152 and a mini-magneticstir-bar were first put into the multi-neck flask. Then one end of the capillaries were inserted through the small rubber seals each with a cut just big enough to receive the capillaries while the other ends were broken open and put into the open necks of the flask. The rubber seals are slightly lubricated so that we can move the capillaries up and down in the flask, while still maintaining a vacuum seal. Before loading the required amount of SCN into the flask, we need to pump the glassware down to vacuum level. But owing to the strong tendency of C152 to sublimate, we chill the flask containing C152 with liquid nitrogen during this evacuating process. We then load a measured amount of SCN from the cylindrical style funnel by briefly opening the threaded teflon valve followed by pumping the glassware again and heating up the SCN/C152 to melt. After sufficiently stirring the SCN/C152 mixture, we dip the open ends of the capillaries (inside the multineck flask) into the material, and after disconnecting the vacuum pump, the flask is slowly filled with helium to push the molten material up the capillaries. We then pull the capillaries up somewhat so that their open ends are out of the liquid and, after the melt in the flask has solidified, the flask is put back under vacuum again. Warming up the open ends of the capillaries with a heat gun we remove all material close to the openings, for about 5-7 cm. We pull the emptied portion of the capillaries halfway out of the flask and then flame sealed them under vacuum. Each capillary is further cut into two pieces by further flame sealing; one, with a length of 16cm, serves as the sample cell for the experiments, and the other short section was used for concentration calibration.

We finally make two samples, one with a relatively high concentration and the other with a relatively low concentration, which are used as the standard samples in calibrating the concentration of all other samples. To achieve accurate concentrations of these two sample, we use sufficiently large amount of SCN and C152 and load them into the capillaries under a nitrogen gas environment. We did not choose to make the two standard samples under vacuum to avoid possible sublimation of C152 which can make the concentration less accurate. The concentrations of all samples are finally calibrated by fluorescence measurements (see section 3.2.4)

3.2.3 Sample Purity and Chemical Stability Test

After loading the four-times vacuum distilled SCN into a cleaned capillary, we immediately perform a purity test (the "Chester Test", originally devised by Chester Qian). We set up a very low temperature gradient (~5 K/cm) and pull the sample at high speeds. For pure samples, there is still no sign of instabilities occurring on the interface, even when the pulling speed has reached 100 μm/s. From the analysis leading to Figure 20a, we can estimate the upper limit for remaining impurity concentration as $c \leq 0.01$ wt%.

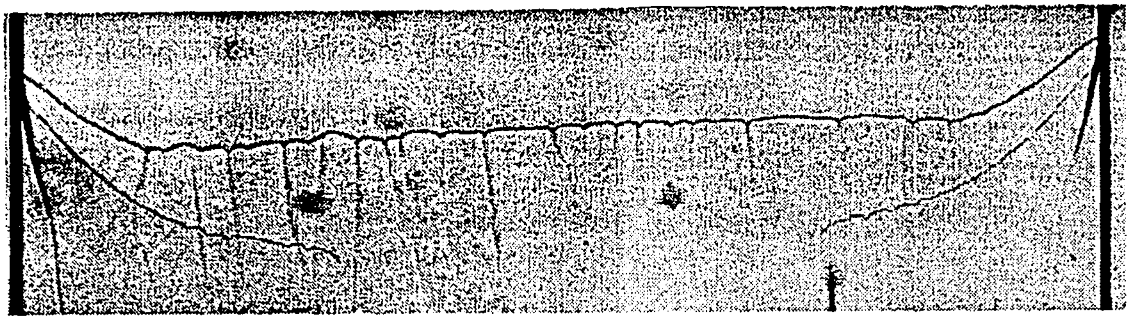

Figure 26 Succinonitrile purity test. (SCN, four time vacuum distilled, loaded into cleaned capillary under vacuum, G=10 K/cm, V=98.93 mm/s)

Another consideration of concern for the SCN/C152 mixture is the chemical stability of the laser dye C152 since it has a tendency to exhibit decomposition due to environment changes after some time. We have conducted tests of the critical velocities for the same SCN/C152 samples after an 18 month interval and no differences were detected. We therefore concluded that when subjected to the conditions of our experiments these samples are chemically stable.

3.2.4 Measurements of the Thermodynamic Parameters of SCN/C152.

The first measurements conducted on the SCN/C152 samples was to calibrate their concentration by fluorescence measurements. We produced a set of SCN/C152 samples as described in section 3.2.2, with C152 concentrations that, according to these fluorescence measurements, ranged from 0.01 to 0.430wt%.

We also determined the partition coefficient *k* [77] and the solute diffusion constant *D* by fluorescence measurements[78]. To measure the partition coefficient *k* a sample with known concentration (we used SCN/C152 with C152 concentration at 0.430 wt%) was pulled for a short time at low pulling speed in the directional solidification apparatus to establish a region of the sample having a uniform coumarin concentration. The growth time and pulling speed was chosen so that the solute concentration ahead of the advancing solidification front did not build up significantly before the growth was stopped. The sample was then allowed to equilibrate for several days. An incident laser beam with low intensity (to avoid melting the solid) was focused on the solid and liquid side of the sample alternately for the same period of time (typically 1-2 minutes). The fluorescent intensity was measured by accumulating photocounts from a photomutiplier. The fluorescence intensity I is verified experimentally to be proportional to the concentration c for c up to about 1wt%, and the fluorescent efficiency is the same for both solid and liquid. The background intensity caused by scattering from the windows and surfaces of the capillary was measured by performing the measurement with a pure SCN sample. After subtraction of the background intensity, the partition coefficient k was determined as $k = I_{solid}/I_{liquid}$.= 0.05 ± 0.01. To determine D, a similar low intensity laser beam was focused on the solid side of the sample. We then suddenly increased the temperature of the hot block so that the solid where the laser light was focused became liquid. The coumarin diffusion into the low concentration region previously occupied by the solid was monitored by the increase of fluorescent intensity I since $I \propto c$. The diffusion coefficient D was then extracted from fits to the time dependent solution of the diffusion equation for an initial concentration step at $z = 0$:

$$c(z,t) = c_S + 0.5(c_L - c_S)erfc(z / \sqrt{4Dt}) \tag{3.1}$$

where c_L and c_S are the initial coumarin concentration in the liquid and solid respectively.

To determine the liquidus slope m, we first slowly pulled an empty capillary with a thermister attached across the gap between the hot and cold blocks. We mapped out the temperature profile along the z-direction inside the stainless steel tunnel. We then put all the SCN/C152 samples into the apparatus to obtain their interface positions under the same temperature gradient after allowing them to completely equilibrate, and subsequently obtained the melting temperature of each sample by observing its interface position on the temperature field plot across the gap. We were then able to plot the melting temperature of each sample against its concentration; the slope of this curve gives the value of *m*, the slope of the liquidus curve.

A summary of the thermodynamic parameters of SCN/C152 and SCN/Acetone systems used in this dissertation is given in the table below.

TABLE I. Values of physical parameters for the SCN/C152 and SCN/Acetone mixtures. Values refer to SCN except where noted otherwise.

Parameter	**Value**	**Reference**
MW-SCN (g)	80.092	79
MW-C152 (g)	257.20	Sigma Chemical Co.
ρ_S (g/cm^3)	1.034 at 25 ^{0}C	79
(Density of Solid.)	1.023 at 45 ^{0}C,	79
	1.016 at 58 ^{0}C	80
ρ_L (g/cm^3)	0.970 at 58^{0}C	80
V_S (cm^3) (molar volume of solid)	78.83 at 58^{0}C	80
V_L (cm^3) (molar volume of liquid)	82.54 at 58^{0}C	80
ΔV (molar volume change in melting)	3.71	79
n_S refractive index of solid	1.4320	81
n_L (refractive index of liquid)	1.4172	81
T_M (K)	331.25	81
L (J/cm^3)	45.7	33
	(47.8)	79
C_S (cal/mole-K)	36.56 at 52 ^{0}C	79
C_L (cal/mole-K)	38.37 at 62 ^{0}C	79

D_{th}' (cm^2/s)	1.14 x 10^{-3} at 58 ^{0}C	$D'_{th}=K'_{th}/(C_S\rho_S)$
D_{th} (cm2/s)	1.16 x 10^{-3} at 58 ^{0}C	$D_{th}=K_{th}$ /($C_L\rho_L$)
K'_{th} (cal/cm.s.^{0}C)	(5.36 ± 0.05) x 10^{-4} at 58 ^{0}C	81
K_{th} (cal/cm.s.^{0}C)	(5.32 ± 0.15) x 10^{-4} at 58 ^{0}C	81
γ (J/cm^3) (surface energy)	(8.94 ± 0.5) x 10^{-7}	81
D (cm^2/s) (diff. coefficient of C152)	(2.5 ± 0.1) x 10^{-6}	This work
k (SCN/C152)	0.05 ± 0.01	This work
m (K/wt%) (SCN/C152)	1.65 ± 0.25	This work
D (cm^2/s) (SCN-Acetone)	1.27 x 10^{-5}	33
k (SCN/Acetone)	0.1	33
m(K/wt%)(SCN/Acetone)	3.02	33

3.3 Data Acquisition and Image Processing

The video microscopy technique was employed in this research. As shown in Figures 21 and 22, the directional solidification apparatus is mounted on the stage of a Nikon Diaphot inverted microscope. We use a 10x long working-distance objective and a 1x projection lens in the video port. The image of our crystal interface is recorded by a Dage MTI CCD-72 video camera which provides almost distortion-free images (a calibration has previously been made for all choices of magnifications used in this lab.). The CCD camera is interfaced to a digital image processing board (Data Translation DT2255 Quick Capture board) in a Mac II computer and provides digitized images consisting of 640x480 pixel spatial resolution and 256 shades of gray at 30 frames/s. One pixel corresponds to an area of approximately 2 x 2μm in the sample at magnification of 4.

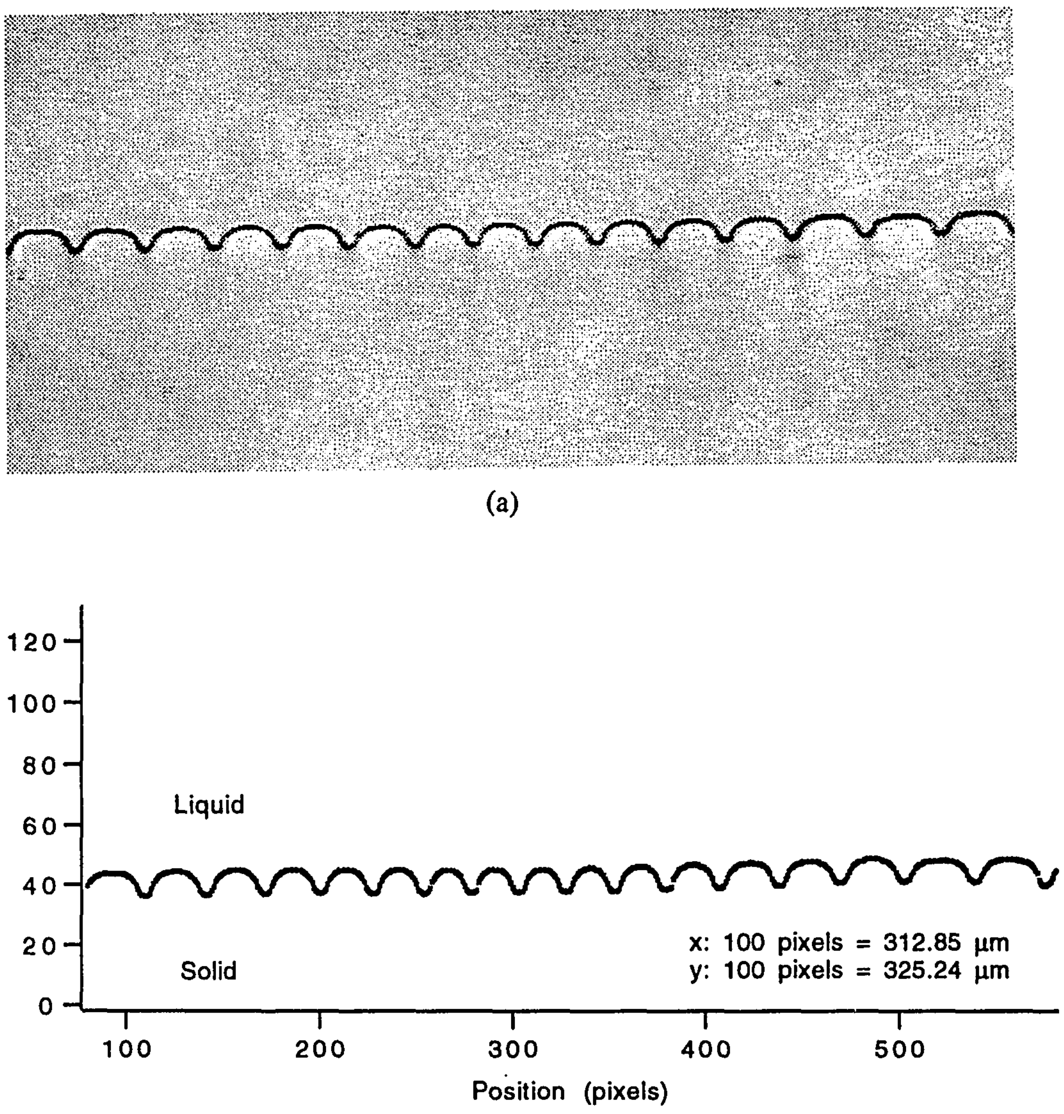

(a)

(b)

Figure 27 A cellular interface profile: (a) video image. (b) Interface profiles extracted from (a).

The digitized images are further processed using two commercial image analysis programs -- *Image (NIH)* and *Enhance*, and with customized C-programs written in our laboratory. Our programs are intended to extract digital interfaces for accurate quantitative analysis (see Figure 27). The video images of the interfaces are digitized by the QuickCapture video board with 640 x 480 pixel spatial resolution and 256 gray scales on the computer screen. Each image point is characterized by a triplet of integers (x,y,I) where (x,y) are its coordinates in units of pixels (0-640, 0-480) and I is its intensity value (from 0 to 256). A subroutine named "ReadTiff.c" was employed to perform the task of opening the image files which were saved in the Tiff format during the experiments, reading their header information and transferring the image data into computer memory for further processing. We set an intensity threshold with value between the intensity value of the pixels on the interface and the intensity value of the pixels on the background. We then scan the interface region with scan lines perpendicular to the interface. The position of the interface was extracted from the intensity profile along each scan line by parabolic fitting. (see Appendix B).

4. Experiments and Results

4.1 *Subcritical-Supercritical Bifurcation Crossover*

4.1.1 Experimental Procedures

Exploiting the optical absorption of the laser dye C152 used as the second component, the laser-fiber coupling mechanism was employed to obtain a single well oriented crystal because defects and grain boundaries can modify the planar-cellular transition.[82,83] After the initial solidification, we used the laser to melt all the grains except one, which was then melted back to provide a small seed for initiating crystallization. This procedure was repeated until a single well-oriented crystal was obtained.[84] Once a suitable seed was obtained, the sample was left in the apparatus for several days with the entire liquid side of the sample molten to allow the dye distribution to equilibrate.

The experiments were carried out in a temperature gradient of either 52 or 100 K/cm with pulling velocities ranging from 0.05 to 15 μm/s. During a run, it is important to allow the interface to reach equilibrium at each pulling speed. Several precautions were taken to ensure this: grain boundaries must be eliminated, the seed crystal must be precisely aligned both vertically and horizontally, the impurity must be uniformly distributed, and, most important of all, the sample must be kept long enough at each pulling speed. To ensure the last condition, each pulling speed was individually tested and maintained for up to six hours. Then for a complete run, the pulling speed V was increased gradually in small increments (typically 0.03 μm/s) and the typical waiting times between V

steps were ~2 hours. After the planar interface became unstable at $V \sim V_C^+$, the pulling speed was increased well above V_C^+ in several steps to make sure that the system entered the cellular regime completely; V was then slowly decreased in small increments until a cellular-planar bifurcation occurred at $V \sim V_C^-$. The interface profile was recorded continuously with a VCR.

4.1.2 Hysterisis

The observed hysteresis $\Delta V = V_C^+ - V_C^-$ at G=52 K/cm for all samples are shown in Figure 28. Different symbols represent individual experimental runs. The five groups of points correspond to c = 0.019, 0.062, 0.130, 0.236 and 0.301wt%. For the c = 0.019 and 0.062 wt% samples, $\Delta V = 0$ within experimental error. The solid curve was calculated from equation (2.111) using measured thermodynamic parameters for SCN/C152 to compute a_0 and a_1, with a_2 arbitrarily fixed at 400. The scatter observed in different runs for a particular sample is expected, since ΔV_{max} of equation (2.111) is merely an upper limit to ΔV_{expt}. In calculating the slope $s = da_0/dV$ at V_C, we first find the wave number corresponding to the most unstable mode which is related to the peak position in Figure 10 from the linear stability analysis equation (2.35); then upon substituting q by V and c we obtained the linear growth rate a_0 as a function of the pulling speed V and solute concentration c at the most unstable mode. The slope $s = da_0/dV$ was then derived at $V=V_C$ (see Figure 12). In plotting Figure 28 we used the simplified equation for a_1 (equation 2.110). For higher concentration samples, the pulling speed is relatively low and the latent heat is not so important. For these samples, the experiments always show some velocity hysteresis region, characteristic of a subcritical bifurcation, as was also found by other researchers [85,86,87,88] for other binary systems. But when the solute concentration decreases, the critical pulling speed increases and the thermal field becomes increasingly important. The experiments show that with decreasing *c* the size of the hysteresis region decreases monotonically and eventually vanishes, as predicted by Merchant and Davis. In other words, a bifurcation transition from subcritical ($a_1<0$) to supercritical ($a_1>0$) has indeed taken place. The crossover (at $a_1 = 0$) occurs at a concentration of $c_t \sim 0.1$ wt%, which agrees with the calculation from the full a_1 expression (equation (2.107)) using measured thermodynamic parameters (TABLE 1).

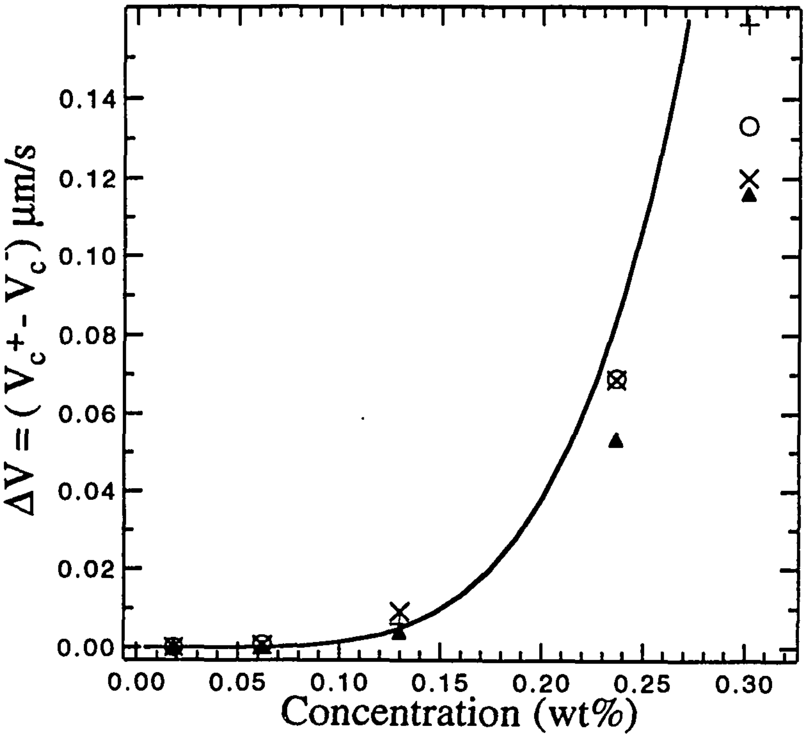

Figure 28 The observed hysteresis points and the theoretically predicted hysteresis line.

It must be noticed that the above theoretical calculations employed the physical parameters for the SCN/C152 mixture that are based on the existing measurements by other authors and by ourselves (Table 1). Comparing the strict requirements for the subcritical and supercritical bifurcation experiments, the precision of these previously measured parameters are far from satisfying. We have confidence in determining the partition coefficient *k* and the solute diffusion coefficient *D* for the SCN/C152 mixture by using the fluorescence measurement but *m* can only be determined preliminarily in the way we presented, because the accuracy of *m* depends on the accuracy of the solute concentration calibration and the melting temperature determinations. Some crucial

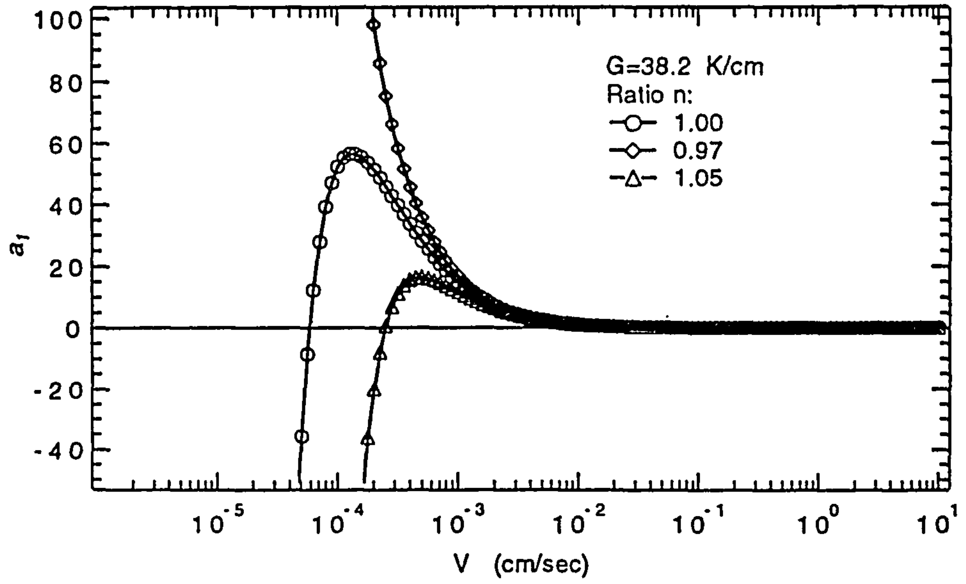

Figure 29 The Landau coefficient a_1 vs the pulling speed V from equation (2.107) with different values of the ratio of thermal conductivities ($n=K_{th}'/K_{th}$) for SCN-Acetone at G=38.2 K/cm.

thermodynamic parameters, in particular the thermal conductivities $K_{th}(K_{th}')$ were obtained in earlier work as a peripheral result while measuring other parameters [81] and include large uncertainties. These uncertainties can significantly influence the value of a_1.

In Figure 29, we have plotted the Landau coefficient a_l vs the pulling speed V (equation 2.107). We chose three values of the ratio of the thermal conductivities n within the uncertainty range of previously measured value of K_{th} and K_{th}', n=1.007±0.037 (see TABLE 1). These values of n drastically affect the crossover values of subcritical to supercritical bifurcations where a_1 changes sign from negative to positive, making the theoretical predictions of the crossover unreliable.(Note that for $n < 1$, there is no crossover.) Most measurements of these thermodynamic parameters were performed nearly twenty years ags. These measurements are difficult and require special equipment. We realize that a more accurate and systematic measurement of these parameters will be necessary in order to properly compare theoretical predictions and experimental results.

4.1.3 Amplitude for V Near or above V_C^+

When the pulling speed V reaches V_C^+, the planar interface becomes unstable; the instability was observed to originate in one or more localized regions and spread laterally across the interface, finally restablizing to a cellular interface. The spreading occurs more rapidly for the higher concentration samples. Figure **30** shows the interface profiles after restablization following the initial instability for four samples with c = 0.019, 0.062, 0.130, 0.236 wt%, with G = 100 K/cm. Their critical velocities are 13.15, 7.282, 2.311. and 1.324 µm/s. The top reference image is of a planar interface at rest. At low concentrations the cellular interface restablizes at very small amplitudes as expected for a supercritical bifurcation, while at high concentrations a large amplitude cellular pattern appears, characteristic of a subcritical bifurcation. Also, as previously found by other authors, once the pulling speed is above V_C^+ at a subcritical bifurcation, the amplitude grows nonlinearily with increasing V which indicates that the system has entered a nonlinear regime and the Mullins-Sekerka theory no longer applies.

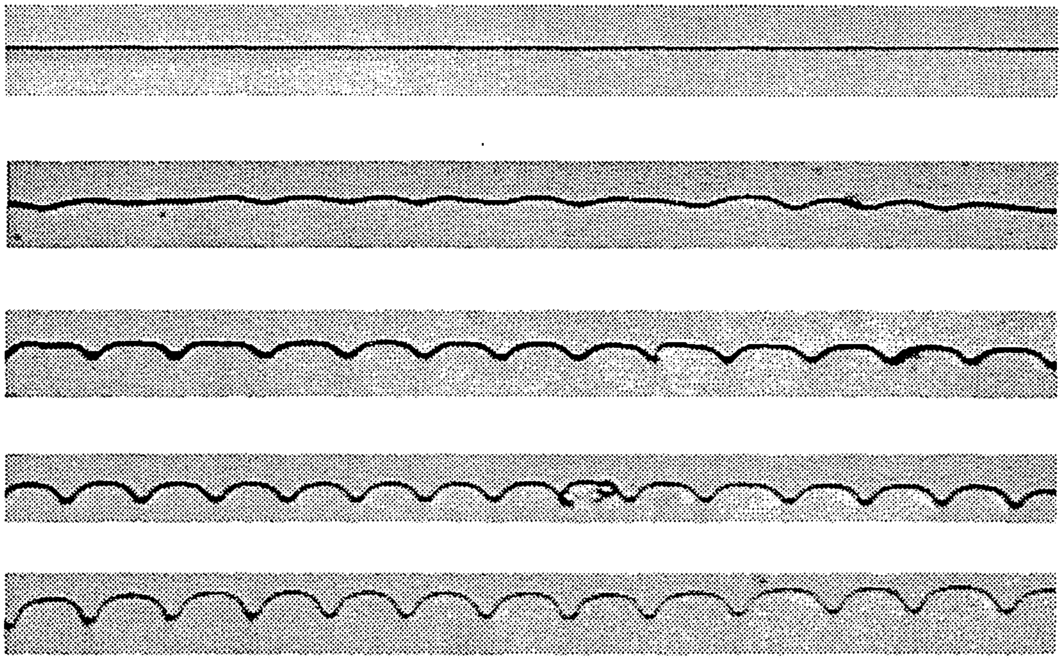

Figure 30 Interface profiles after restablization following the initial instability. The top reference image is of a planar interface at rest. The four following images are for c = 0.019, 0.062, 0.130, and 0.236 wt%, with G = 100 K/cm.

Once the pulling speed is above the critical velocity the experiments also indicated that, in the case of supercritical bifurcations, the amplitude grows roughly following $(V-V_C)^{1/2}$ as predicted by the theory and by previous experiments[89].

4.1.4 Wavelength Selection

The measured wavelengths at the initial instability ranged from 89μm (c = 0.19 wt%) to 107μm (c = 0.236 wt%). The Mullins-Sekerka prediction for this system at the given conditions ranged from 118 ~ 179 μm which is ablout ~1.5 times larger, as found in previous experiments. [85,86,90] Once $V > V_C^+$, the wavelength decreases as the pulling speed increases; conversely, the wavelength increases when the pulling speed decreases. Figure 31 shows the wavelength of a cellular interface of the SCN/C152 sample with 0.0621 wt% C152 concentration for five values of pulling speed V at 7.085 μm/s, 8.856 μm/s, 8.856 μm/s, 9.84 μm/s, 7.872 μm/s (from (a) to (e)). For this sample, the critical velocity is at 6.951 μm/s with G = 80 K/cm. Once the system entered the cellular regime, we continuously varied the pulling speed by first increasing and then decreasing the speed for several steps ((a) to (e) in Figure 31). In Figure 31, (b) indicates a transient state during the velocity change from 7.085 to 8.856 μm/s while the other figures indicate that a steady state has been reached. It was found in the experiments that the wavelength adjustments occur in the following ways: (1) one or more cells die out, (2) a cell grows from a relatively big cell, or, (3) tip splitting of several cells occurs at the same time. It was also observed in the experiments, when V is above V_C^+ but the system was still in the cellular regime, that for a relatively large step increase of V the initial cellular pattern may first undergo a wavelength decrease (the number of cells increases) and a significant increase of the amplitude; but then the system tends to readjust spontaneously back to a

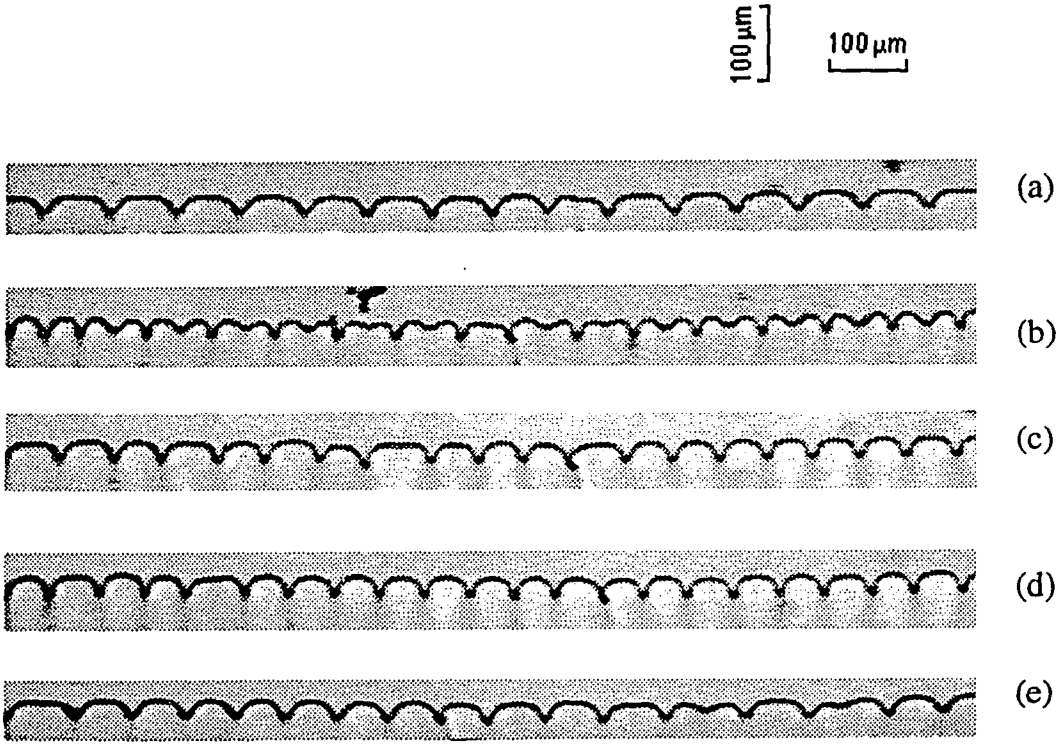

Figure 31 Wavelength of a cellular interface vs a continuous change of the pulling speed V. SCN/C152, c=0.0621wt%, G=80 K/cm. V_c=6.951μm/s. (a) V=7.085 μm/s, (b) V=8.856 μm/s, (c) V=8.856 μm/s, (d) V=9.84 μm/s, (e) V=7.872 μm/s.

bigger wavelength and smaller amplitude. Conversely, if the system was initially at a deep cells stage, a large step of V decrease can bring the interface pattern to a very small amplitude cellular pattern and the wavelength appears to be large but after a transient the interface returns to an intermediate size cells with smaller wavelength. A decrease of V to below V_C^- brings the cellular interface to a steady state planar interface in subcritical bifurcation case.

At the onset of instability, regardless of the nature of the bifurcation, the initial wavy pattern exhibits an experimentally reproducible wavelength. As the velocity is increased, it is found experimentally that the wavelength always decreases, suggesting a selection curve in the velocity-wave number plane (Figure 11). This curve resembles the curve of the fastest growing modes, but does not generally agree with it quantitatively. Furthermore there is evidence that it can depend on initial conditions and that no selection mechanism exists [11]. Here we will not discuss the general question of wavelength selection since it is still unresolved and remains one of the major challenges of nonlinear dynamics.[11, 91, 92]

4.2 Local Heat Perturbation to a Metastable Planar Interface

4.2.1 Experimental Procedures

Having determined the metastable velocity region of the sample, we then began a preliminary study of the response of the planar interface to a laser perturbation. To provide the perturbation, short pulses of laser light were focused on the interface to create an indentation. The light source was a Spectra Physics 165 Argon laser operating at 457.9nm. The laser output beam, after traversing an electronic shutter, was transmitted through a 8.7-μm inner-core-diameter optical fiber to a focusing lens mounted above the microscope stage. This lens produces a spot approximately 10μm in diameter in the sample. The power output from the lens is ~10 mW. The pulling speed was set in the metastable region $V_C^- < V < V_C^+$ and was gradually increased by small steps. Once the interface had reached equilibrium at each velocity step, a laser pulse was applied to the interface to create an indentation. We then observed the system's reaction to this heat perturbation. This process was repeated for different pulling speeds (still within the metastable region), and for different pulse durations (from 10-30 seconds). For all experiments, the power output from the lens was maintained at ~10 mW.

4.2.2 The Interface Reaction to the Perturbing Instability

The local heat perturbation creates an indentation on the metastable planar interface immediately followed by an initial instability at the indentation. We carried out experiments on a SCN/C152 sample with 0.301 wt% coumarin. With a temperature gradient $G = 101$ K/cm, the critical velocities V_C^- and $V_c{}^+$ were determined to be 0.851 and 1.043 μm/s, respectively.

For velocities just above V_C^- (but far from $V_c{}^+$), the interface responds stably to the perturbation; the interface heals the indentation, i.e. the perturbed interface relaxes back to planar. We first maintained the duration of the laser pulse at 12 seconds with the laser intensity from the fiberoptic head at 8 mW. The pulling speed was varied from V=0.878 μm/s to V= 0.933 μm/s. Although the interface responded to the perturbation

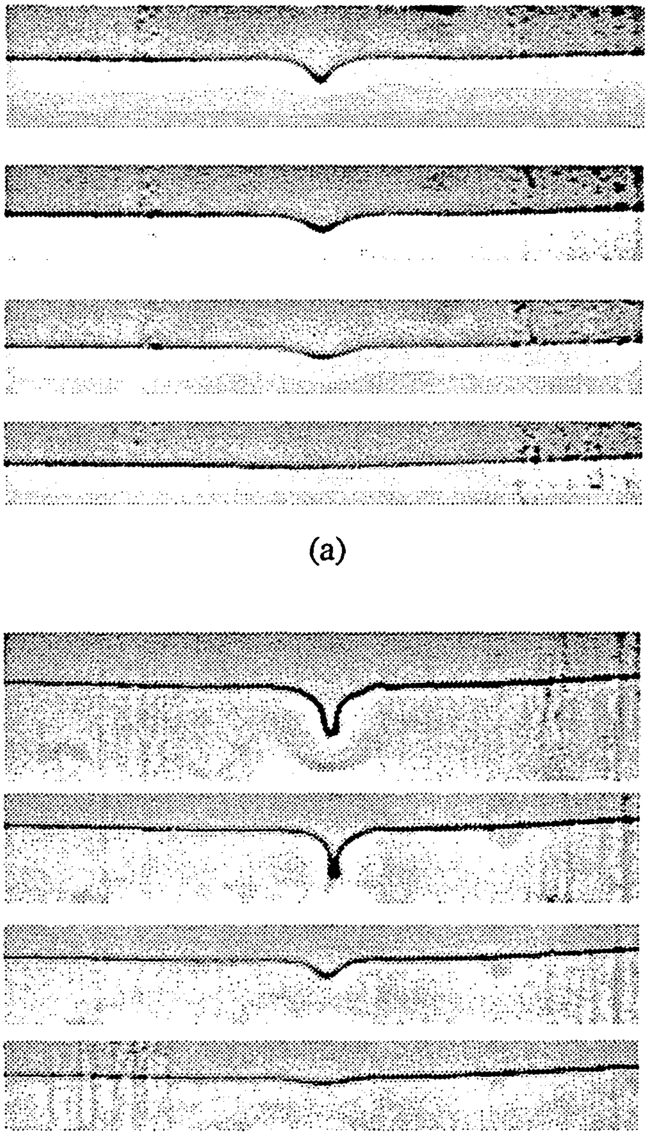

(a)

(b)

Figure 32 The Interface reacts stably to the same perturbation with two different pulling speeds. Pulling speeds are: (a) V = 0.8781 μm/s, (b) V = 0.9330 μm/s; the relaxation times (the time for the planar interface to fully recover from the perturbations) are: (a) 7 minutes, and (b) 14 minutes.

stably throughout this range, the time needed for it to fully recover from the indentation back to the planar steady state was approximately doubled (from 7 minutes to 14 minutes). This process is illustrated in Figure 32 (a) and (b). In this situation the perturbation was simply not strong enough to drive the system from a metastable planar state to the cellular state.

We then maintained the same pulling speed at $V = 0.9330$ μm/s and varied the perturbation intensity by increasing the length of the laser pulse from 12, to 25, to 34 seconds. As observed in Figure 32, increasing the strength of the perturbation in this way also prolonged the relaxation time for the perturbed interface to return to the steady planar state . But the increase was not so significant as in the first case.

The size of the perturbation produced by the laser pulse can be increased by either increasing the duration of the perturbation (as shown in Figure 33) or increasing the pulling speed (as shown in Figure 32). Once the perturbations become sufficiently large, rather than decaying immediately from a shallow and smooth indentation the instability may actually grow for a short time with some initial microstructures at the indentation but eventully vanish (Figure 33)

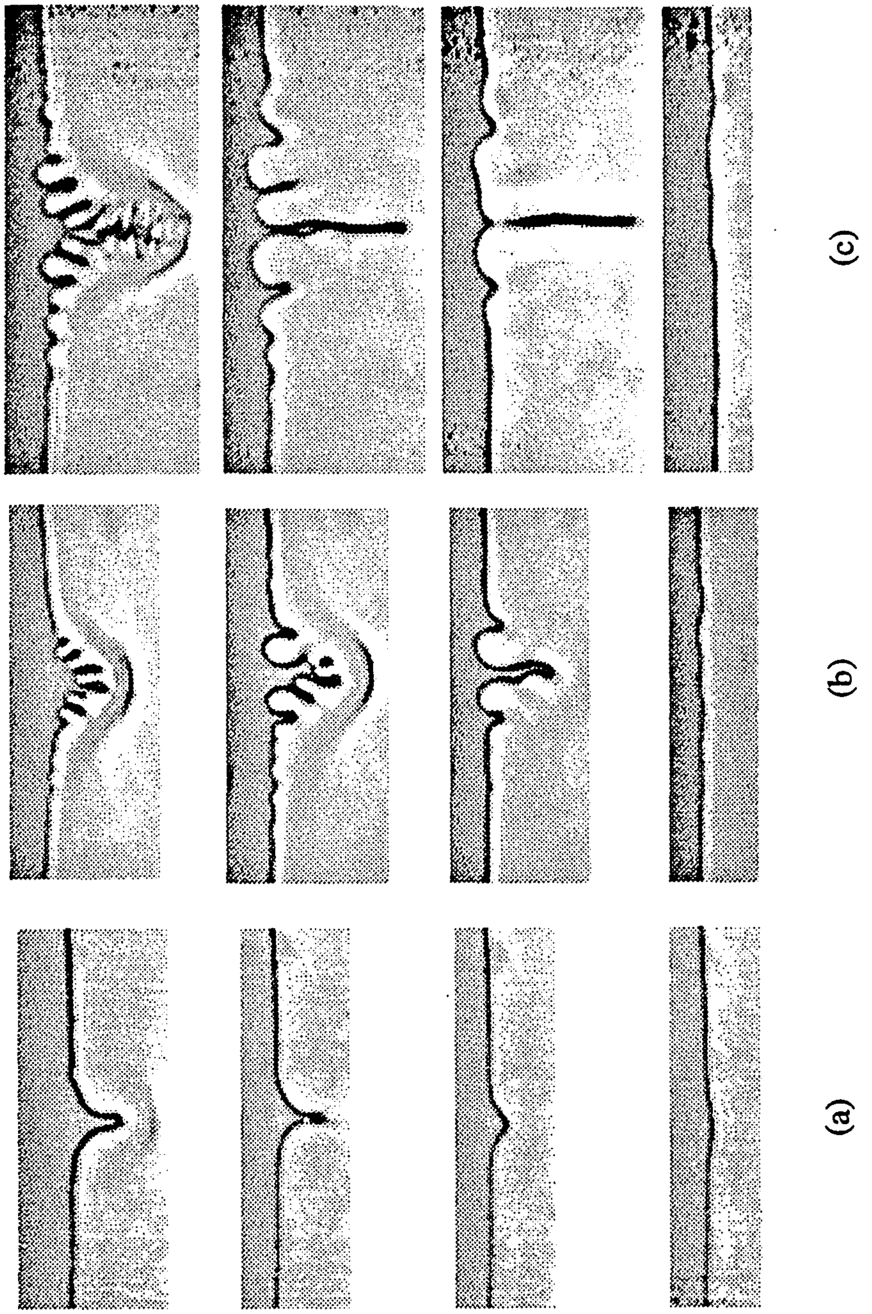

Figure 33 The relaxation time increases as the intensity of the perturbation is increased. Pulling speed is maintained at $V = 0.9330$ µm/s. The perturbation times are: (a) 12seconds, (b) 25 seconds, and (c) 34 seconds. The relaxation times are: (a) 7 minutes, (b) 22 minutes, and (c) 26 minutes.

Increasing the pulling speed gradually towards $V_C{}^+$, we eventually found a different type of behavior in which the initial instability caused by the local heat perturbation grows and the planar interface eventually evolves into a cellular interface

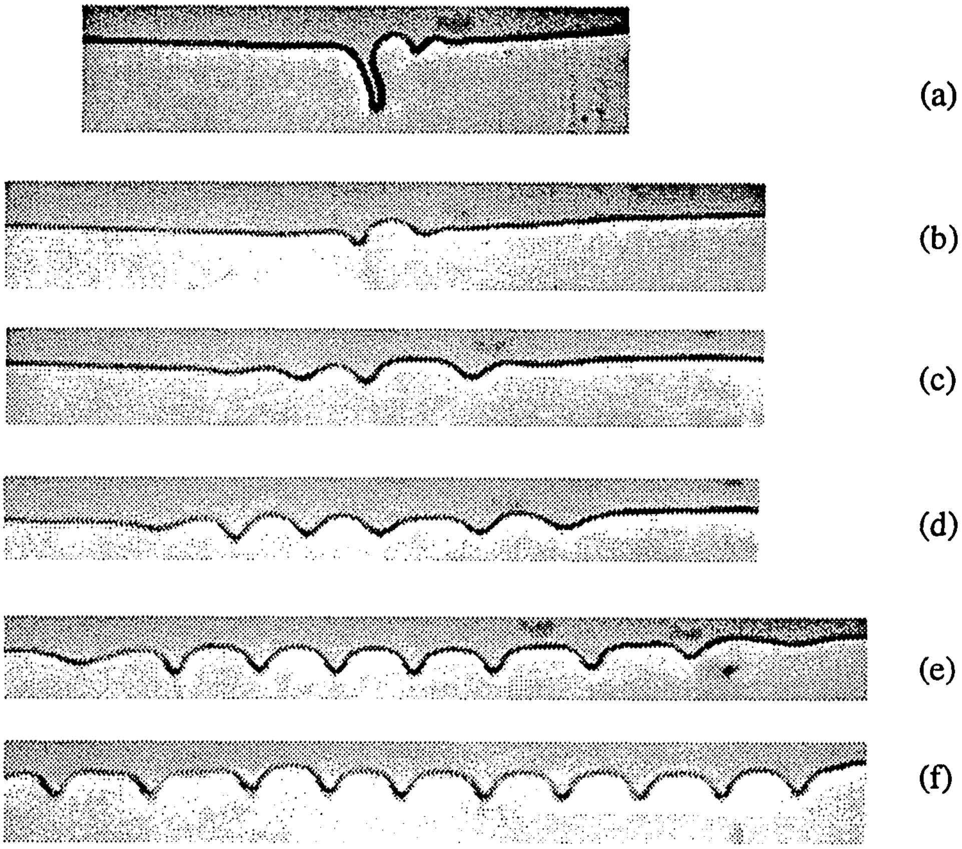

Figure 34 Cells generated by a local heat perturbation spread out across the metastable planar interface. (SCN/C152, c=0.3013 wt%, G=101 K/cm, V = 0.9879 µm/s, $V_C{}^+$=1.0428 µm/s, $V_C{}^-$ =0.8507 µm/s). Perturbation time is 18 seconds. Times after the perturbation are (from (a) to (f)): 1’50”, 4’28”, 17’, 33’43”, 49’43” and 65’38”.

that spreads across the sample even though $V < V_C^+$ (Figure 34). As shown earlier in Figure 15, there are two stable solutions, a planar and a cellular interface solution, co-existing between V_C^- and V_C^+. Both are linearly stable against small perturbations. If the perturbation is large enough, rather than dying out, it will drive the system to the upper branch -- the cellular interface. Dynamically, these two stable solutions each posess a basin of attraction separated by a surface approximately indicated by the dashed line in Figure 15. As the pulling speed increases towards V_C^+, the basin of attraction of the planar interface shrinks, while that of the cellular interface grows. For a given initial perturbation, as indicated in Figure 34, the interface can then more rapidly enter the basin of attraction of the cellular interface solution. Thus the perturbation grows and a cellular to planar invasion occurs, i.e. the cells generated by the local heat perturbation at the indentation spread out laterally across the planar interface. We note that all theoretical analysis of such phenomena is based on small sinusoidal perturbations with a unique wavenumber q, while the perturbation produced in our experiment contains multiple Fourier components. For further experimental study, we plan to replace the simple localized heat pulse with a sinusoidal perturbation produced by crossing two laser beams in the sample to form an interference pattern with adjustable q.

5. Conclusions

The main objectives of this dissertation were to search experimentally for the subcritical to supercritical bifurcation crossover in directional solidification as predicted by Merchant and Davis, and subsequently to investigate the dynamics of pattern formation in the metastable velocity region.

We designed and assembled a directional solidification apparatus based on the concepts of Jackson and Hunt's equipment [6], but including some crucial new features designed to ensure precision, stability and programmable control, especially at extremely low pulling speed and high temperature gradient conditions. A fiberoptic laser perturbation capability was included for studying the response of the interface to externally applied perturbations. Sample preparation and testing procedures were also developed as necessary prerequisites for the difficult planar-cellular bifurcation experiments.

We performed directional solidification experiments on a series of succinonitrile samples containing different concentrations of Coumarin152, and verified that the predicted subcritical to supercritical bifurcation crossover occurs at a concentration $c_t \sim 0.1$ wt%. Preliminary experiments have illustrated a variety of interesting phenomena of the response of a metastable planar interface (i.e. the planar interface at velocities within the hysteresis region that is linearly stable but nonlinearily unstable) to the localized heat perturbations in directional solidification. Further systematic experiments should be continued to explore the dynamics of pattern forming instabilities.

6. Appendix A Algebraic Detail

To obtain dimensionless equations (2.39)-(2.48), we need to replace the physical quantities by their dimensionless correspondences defined in section 2.4.2 in the physical equations (2.1)-(2.9). Following are the steps of deriving equation (2.46) and (2.47).

The interface is at $\underline{z}=\varepsilon\underline{\zeta}$, the unit normal vector **n** is pointing to the liquid side of the interface.

$$\mathbf{n} = (n_x, n_y) = (-\mathrm{Sin}\alpha, \mathrm{Cos}\alpha) = \left(-\frac{d\underline{z}}{\sqrt{d\underline{x}^2+d\underline{z}^2}},\ \frac{d\underline{x}}{\sqrt{d\underline{x}^2+d\underline{z}^2}}\right)$$

$$= \left(-\frac{\underline{z}'}{\sqrt{1+(\underline{z}')^2}},\ \frac{1}{\sqrt{1+(\underline{z}')^2}}\right) = \frac{(\varepsilon\underline{\zeta}_x, 1)}{\sqrt{1+\varepsilon^2\underline{\zeta}_x^2}} \ ,$$

$$V_n = V\bullet\mathbf{n} = \frac{(V+\varepsilon\underline{\zeta}_t)}{\sqrt{1+\varepsilon^2\underline{\zeta}_x^2}} \ .$$

Substitute *V*, **n** and other scaled parameters into equation (2.7), it yields

$$\text{l.h.s.} = LV\bullet n = L\left(V+\frac{\varepsilon(D/V)}{D/V^2}\zeta_t\right)\cdot\frac{1}{\sqrt{1+\varepsilon^2\underline{\zeta}_x^2}} = LV(1+\varepsilon\zeta_t)\frac{1}{\sqrt{1+\varepsilon^2\underline{\zeta}_x^2}} \ ,$$

$$\text{r.h.s} = (K'_{th}(\underline{\nabla T}') - K_{th}(\underline{\nabla T}))\cdot \qquad \frac{T_M K_{th}}{(D/V)}(n(\nabla T') - \nabla T)\cdot\frac{(-\varepsilon\underline{\zeta}_x\vec{e}_x + \vec{e}_z)}{\sqrt{1+\varepsilon^2\underline{\zeta}_x^2}}$$

$$= \frac{T_M K_{th}}{(D/V)}\cdot\left[n\frac{\partial T'}{\partial z} - \frac{\partial T}{\partial z} - \varepsilon\zeta_x\left(n\frac{\partial T'}{\partial z} - \frac{\partial T}{\partial z}\right)\right]\cdot\frac{1}{\sqrt{1+\varepsilon^2\underline{\zeta}_x^2}}$$

By cancelling the common factors on both l.h.s. and r.h.s., we obtain equation (2.46):

$$n\frac{\partial T'}{\partial z}-\frac{\partial T}{\partial z}-\varepsilon\zeta_x\left(n\frac{\partial T'}{\partial z}-\frac{\partial T}{\partial z}\right)=\frac{LD}{T_M K_{th}}(1+\varepsilon\zeta_t).$$

Substituting the dimensionless parameters into equation (2.8), we have

$$T_M T = T_M + mc_0^{\bullet}c+\frac{\sigma}{L}T_M\frac{\underline{z}''}{(1+(\underline{z}')^2)^{3/2}}$$

After some algebra, we obtain equation (2.47):

$$T = 1 + M c + \gamma\,\varepsilon\,\zeta_{xx}\,(1 + \varepsilon^2\,\zeta_x^2)^{-3/2}.$$

In the limit of $a_0 \to 0$, the coefficients of d_1, d_2, d_3, d_4, d_5 which appear in equation (2.104) can be found in reference 12.

The necessary constants A_{ij}, B_{ij} and ζ_{ij} required in calculating a_1 (equation 2.107) are listed below [26] (Note that A_{11} and A_{20} in reference 26 appendix A contained some errors.). Others can be found in reference 24.

$$A_{10}=\frac{-k(k-1)}{2(m_{10}+k-1)},\qquad B_{10}=\frac{(k-1)(n+1)}{4I}-\frac{(n-1)(k-1)G}{4}\quad,$$

$$A_{20}=\frac{k-1}{8}+\frac{m_{10}A_{10}}{2}-\zeta_{20}(k-1)\left(1-G-\frac{4Aq^2}{k}\right)\quad,$$

$$A_{11}=(1-k)\zeta_{11}-\frac{k(k-1)m_{10}}{4(m_{10}+k-1)}+\frac{k-1}{8}\quad,\qquad \zeta_{11}=\frac{q(1-n)}{4(n+1)}+\frac{qI^{-1}}{2(G-I^{-1})(n+1)}\quad,$$

$$\zeta_{20}=\left\{\left[2q^2+m_{10}(1-m_{20})\right]\frac{A_{20}}{2}+\frac{1}{8}(k-1)(1-m_{20})\right\}\cdot$$
$$\left\{(k-1)\left[k-(m_{20}+k-1)\cdot\left(1-G-4q^2\frac{A}{k}\right)\right]\right\}^{-1}$$

Following are algebraic details used in deriving equation (2.111):

We solve for steady-state solutions of the amplitude A from the Landau equation:

$$dA/dt = f(A) = a_0 A - a_1 A^3 - a_2 A^5 + \ldots$$

where $a_1 = a_1(V,c)$, and a_2 is assumed to be a positive constant. In the vicinity of marginal stability, the linear growth rate a_0 can be assumed to be linear in V-V_C:

$$a_0 = a_0(V,c) = s(V - V_C^0)$$

where s is the slope of a_0-V curve at V_C^0.

Three solutions of $dA/dt = 0$ exist for $a_1 < 0$,

$$A_1 = 0, \qquad A_2 = \left(\frac{-a_1 + \sqrt{a_1^2 + 4a_0 a_2}}{2a_2}\right)^{1/2}, \text{ and } A_2 = \left(\frac{-a_1 - \sqrt{a_1^2 + 4a_0 a_2}}{2a_2}\right)^{1/2}$$

These three solutions are indicated in Figure 15 as the bottom planar solution, the upper cellular solution and the dashed line of metastable solution. Stability behavior in each case is determined by the value of df/dA such that:

$$\frac{df}{dA} = \begin{cases} > 0, & \text{instability} \\ < 0, & \text{stability} \\ = 0, & \text{marginal stability} \end{cases}$$

It is obvious that $\left.\frac{df}{dA}\right|_{A_1} = a_0$, with $a_0 < 0$ when $V < V_C^0$ and $a_0 > 0$ when $V > V_C^0$, where V_C^0 is the critical velocity obtained by Mullins-Sekerka linear stability analysis. So V_C^+ is determined by V_C^0. As the velocity is decreased, A_2 decreases and A_3 increases. They reach the same value $A_2 = A_3 = \left(\frac{a_1(V_C^-)}{2a_2}\right)^{1/2}$ at V_C^- when $a_1^2(V_C^-) + 4a_0(V_C^-)a_2 = 0$.

Substituting $a_0(V_C^-) = s(V_C^- - V_C^0)$ into $a_1^2(V_C^-) + 4a_0(V_C^-)a_2 = 0$, we have

$$a_1^2(V_C^-) + 4a_2 s(V_C^- - V_C^+) = 0$$

Thus the maximum possible hysteresis $\Delta V_{\max} = V_C^+ - V_C^-$, set by the limits of stability of the planar and cellular interfaces, is given by

$$\Delta V_{\max} = \begin{cases} \dfrac{a_1^2}{4a_2 s}, & a_1 < 0 \\ 0, & a_1 > 0 \end{cases} .$$

7. Appendix B Computer Programs

The purpose of this program is to perform feature extraction for the planar and cellular interface. It consists of two parts: The main program called "Interfacepar.c" and the subroutine named "ReadTiff.c". They were written in C language using MPW-C (Macintosh Programmer's Workshop). The subroutine ReadTiff.c was written by Martin Muschol and Lloyd William. It performs the task of opening the TIFF files (our images are stored in Tiff format using *Image* during experiments) and access the formating information in it. On return it provides the calling program with a pointer to the beginning of the image data and the horizontal and vertical dimension of the image.

```
/*Name of Program: Interfacepar.c*/

/*This main program extracts the interface profiles. It calculates the features above certain
threshold and determines the interface coordinates using parabola fits.*/
#include        <stdio.h>
#include <math.h>
void    ReadTiff(char *, unsigned char **,unsigned short *,unsigned short *);
main (argc,argv)
int argc;
char **argv;
{
        FILE *filePtr;
        int     wFlag,toppix,botpix,xpix[640],ypix[640],*xpix_ptr,*ypix_ptr;
        unsigned char           *mptr;          /* memory pointer to image   */
        unsigned short          hor,ver,box_size; /*horizontal & vertical dimension of
image */
        int                     npts;
        float           *interface_ptr;
        int             getmax() ;
        int             j;
        extended        yypix[640],*yypix_ptr;
```

```
/* Check if the input line contained the name of the program,the names of the two
output files and a value for the threshold. If not, exit to shell */
        if (argc != 3)
        {
                puts("\r Usage: extract imagefile datafile");
                exit(1);
        }

        printf("\n Enter the range of pixels over which you will scan:");
        printf("\n Top pixel first\n");
        scanf("%d", &toppix);
        printf("\n Now set the bottom pixel\n");
        scanf("%d", &botpix);
        printf("\n I read top = %d bottom = %d",toppix,botpix);

        xpix_ptr=xpix;
        ypix_ptr=ypix;
        yypix_ptr=yypix;

        for (j=0;j<640;j++)
                {
                *(xpix_ptr+j)=0;
                *(ypix_ptr+j)=0;
                *(yypix_ptr+j)=0;
                }

        ReadTiff(argv[1],&mptr,&hor,&ver);
        puts("\n I left ReadTiff");
        npts = getmax(mptr,hor,ver, toppix,botpix,xpix_ptr,ypix_ptr,yypix_ptr);
         if ((filePtr = fopen(argv[2],"w"))==NULL)
        {
        printf("\n I couldn't open the file named  %s",argv[2]);
        exit(1);
        }
```

```
        for(j=0;j<hor; j++)
        {
         if( (wFlag=fprintf(filePtr,"%d   %g \n",*(xpix_ptr + j),*(yypix_ptr + j)))<=0)
                {
                printf("\n a writing error occured");
                }
        }
        }


/*This segment takes a image of (hor x ver) pixels, and set the new intensity of the pixel
to one if the original intensity at that point > threshold, and the new intensity to zero
if the original intensity < threshold. */


int getmax(image_ptr, hor,ver, toppix,botpix,xpix_ptr,ypix_ptr,yypix_ptr)
unsigned char           *image_ptr;
unsigned short          hor, ver,toppix,botpix;
int                     *xpix_ptr,*ypix_ptr;
extended        *yypix_ptr;
{
        unsigned short                  i,j;
        int                             intmax,k,intpos;
        extended sx,sx2,sx3,sx4,sy,syx,syx2,detb,detc,coord,intensity;
        sx =0; sx2 = 0; sx3 = 0; sx4 = 0;
        sy = 0;  syx = 0; syx2 = 0; detb = 0; detc = 0;
        printf("\n hor= %d ver= %d top pix= %d bottom pix= %d",hor,ver,toppix,botpix);
        k=0;
        for(i=0;i<hor; i++)
                {
                intmax=0;
                for (j=botpix; j<toppix; j++)
                        {
                        if(*(image_ptr+ (j* hor)+i) > intmax)
                                {
                                *(ypix_ptr+i)= j;
```

```
                intmax=*(image_ptr+ (j* hor)+i);
                }
            }
            *(xpix_ptr+i)= i ;
            printf("\n col %d row %d int %d", *(xpix_ptr+i), *(ypix_ptr+i),
            intmax);
            intpos=*(ypix_ptr+i);
                printf("\nintpos %d",intpos);
                for (j=intpos-1; j<intpos+2; j++)
                {
                coord=(extended)(j);
                intensity=(extended)(*(image_ptr+ (j* hor)+i));
                sx += coord;
                sx2 += pow (coord,2.);
                sx3 += pow (coord,3.);
                sx4 += pow (coord,4.);
                sy += intensity;
                syx += intensity*coord;
                syx2 += intensity*pow(coord,2.);
                }
        detb = -sy*(sx*sx4-sx2*sx3)+syx*(3.0*sx4-sx2*sx2)-
        syx2*(3.0*sx3-sx*sx2);
        detc = sy*(sx*sx3-sx2*sx2)-syx*(3.0*sx3-sx*sx2)
        +syx2*(3.0*sx2-sx*sx);
            *(yypix_ptr+i)= -.5*detb/detc;
        sx =0; sx2 = 0; sx3 = 0; sx4 = 0;
        sy = 0;  syx = 0; syx2 = 0; detb = 0; detc = 0;
            }
    return(k);                  /* number of points extracted*/
}
```

****

The subroutine named "ReadTiff.c" was written by Martin Muschol and Modified by Lloyd Williams. Details ignored here.

8. References

---

[1] J. Kepler, De Nive Sexangula, 1611. Translated by C. Hardie, Clarendon, Oxford, 1966.

[2] W. Kurz and D.J. Fisher, Fundamentals of Solidification, TransTech Publications, Switzerland, 1984.

[3] J.S. Langer, Physics Today, 45, 24 (Oct. 1992)

[4] P. Haasen, Physical Metallurgy, Cambridge University Press (1986)

[5] B. Chalmers, Principles of Solidification, Wiley New York (1964)

[6] K.A. Jackson and J.D. Hunt, Trans. Met. Soc. AIME 236, 1129(1966)

[7] J.S. Langer, Rev. Mod. Phys., 52, 1 (1980)

[8] J. Flesselles, A.J. Simon and A.J. Libchaber, Advances in Phys., 40, 1 (1991)

[9] P. Haug, Phys. Rev. A 35, 4367 (1987)

[10] W.W. Mullins and R.F. Sekerka, J. Appl. Phys. 35, 444 (1964)

[11] M. Ben Amar and B. Moussallam, Phys. Rev. Lett. 60, 317 (1988)

[12] B. Caroli, C. Caroli and B. Roulet, J. Phys. (Paris) 43, 1767 (1982) (This paper contained a minor error, subsequently corrected by Wollkind et al. [65] , which does not change the qualitative conclusions.)

[13] D.J. Wollkind and L.A. Segel, Philos. Trans. R. Soc. A 268, 351 (1970)

---

[14] J.S. Langer and L.A. Turski, Acta Metall. 25, 1113 (1977)

[15] L.H. Ungar and R.A. Brown, Phys. Rev. B 29, 1367 (1984)

[16] P.C. Hohenberg and M.C. Cross, Fluctuations and Stochastic Phenomena in Condensed Matter, edited by L. Garrido, (Springer, New York, 1987)

[17] S.de Cheveigne, C.Guthmann and M.M. Lebrun, J. Crystal. Growth 73, 242 1985

[18] S.de Cheveigne, C.Guthmann and M.M. Lebrun, J. Phys. (Paris) 47, 2095 (1986)

[19] M.A. Eshelman and R. Trivedi, Acta Metall. 35, 2443 (1987)

[20] J. Bechhoefer, P. Oswald, A. Libchaber and C. Germain, Phys. Rev. A 37, 1691 (1988)

[21] S.de Cheveigne, C. Guthmann, P. Kurowski, E. Vicente and H. Biloni, J. Cryst. Growth 92, 616 (1988).

[22] J.T.C. Lee and R.A. Brown, Phys. Rev. B 47, 4937 (1993)

[23] P.E. Cladis, P.L. Finn and J.T. Gleeson, in *Nonlinear Evolution of Spatio-Temporal Structures in Dissipative Continuous Systems*, edited by F.H. Busse and L. Kramer (Plenum Press, New York, 1990), p.457.

[24] J.I.D. Alexander, D.J. Wollkind and R.F. Sekerka, J. Cryst. Growth 79, 849 (1986).

[25] G.J. Merchant and S.H. Davis, Phys. Rev. Lett. 63, 573 (1989).

[26] G.J. Merchant and S.H. Davis, Phys. Rev. B 40, 1140 (1989)

[27] M.A. Eshelman and R. Trivedi, Scripta Metallurgica 22, 893 (June 1988)

[28] P.E. Cladis, J.T. Gleeson and P.L. Finn, Nonlinear Structures in Physical Systems: Pattern Formations, Chaos and Waves. Proceeding of the second Woodward conference, edited by Lui Lam and H.C. Morris. Spring-Verlag, p55-67 (1990)

[29] P. Kurowski, C. Guthmann and S de Cheveigne, Phys. Rev. A 42, 7368 (1990)

[30] A. Karma, Phys. Rev. Lett. 57, 858 (1986)

[31] N. Ramprasad, M.J. Bennett and R.A. Brown, Phys. Rev. B 38, 583 (1988)

[32] J.D. Weeks and W. van Saarloos, J. Cryst. Growth 112, 244 (1991)

[33] S. de Cheveigne, C. Guthmann, P. Kurowski, E. Vicente and H. Biloni, J. Cryt. Growth 92, 616(1988)

[34] P.J. Braun and S.H. Davis, J. Cryt. Growth 112, 670 (1991)

[35] D.A. Kessler and H. Levine, Phys. Rev. A 41, 3197 (1990)

[36] P. Coullet and G Iooss, Phys. Rev. Lett. 64, 866 (1990)

[37] W. Kurz, W. Giovanola and R. Trivedi, Acta Metallurgica 34, 823 (1986)

---

[38] A. Karma and P. Pelce, Phys. Rev. A 41, 6741 (1990)

[39] M.J. Bennett and R.A. Brown, Phys. Rev. B 39, 11705 (1989)

[40] J.S. Langer, Metall. Trans. 15A, 961 (1984)

[41] R. Pieters and J.S. Langer, Phys. Rev. Lett. 56, 1948 (1986).

[42] R. Pieters and J.S. Langer, Phys. Rev. A 37, 3126 (1988).

[43] M.N. Barber, A. Barbieri and J.S. Langer, Phys. Rev. A 36, 3340 (1987).

[44] Peter Hung, Phys. Rev. A 35, 4364 (1987)

[45] J.D. Weeks and W. Saarloos, Phys. Rev.A 42, 5056 (1990)

[46] H.R. Schober, E. Allroth, K. Schoeder and H. Muller-Krumbhaar, Phys. Rev. A 33, 567 (1896).

[47] J.T. Gleeson, P.L. Finn and P.E. Cladis, Phys. Rev. Lett. 66, 236 (1991)

[48] X.W. Qian and H.Z. Cummins, Phys. Rev. Lett. 64, 3038 (1990).

[49] L.M. Williams, M. Muschol, X. Qian, W. Losert and H.Z. Cummins, Phys. Rev. E 48, 489 (1993)

[50] J. Stefan, "Uber Einige Problem der Theorie der Warmeleitung", S.B. Wien. Akad.Math. Natur. 98, 473 (1889)

[51] S.R. Coriell, G.B. McFadden and R.F. Sekerka, Ann. Rev. Mater. Sci. 15, 119 (1985)

[52] D.S. Riley and S.H. Davis, IMA J. Appl. Math. 45, 267 (1990)

[53] G.B. McFadden and S.R. Coriell, Phys. of Fluids 30, 659 (1987)

[54] B. Caroli, C. Caroli, C. Misbah and B. Roulet, J. Phys. (Paris) 46, 401 (1985)

[55] L.H. Ungar, M.J. Bennett and R.A. Brown, Phys. Rev. B 31, 5923 (1985)

[56] A.A. Wheeler and K.H. Winters, Communicaitons in Applied Numerical Methods 5, 309 (1989)

[57] L.H. Ungar and R.A. Brown, Phys. Rev. B 29, 1367 (1984)

[58] P. Haug, Phys. Rev. A 40, 7253 (1989)

[59] A. Barieri, D.C. Hong and J.S. Langer, Phys. Rev. A 35, 1802 (1987)

[60] A. Karma, Phys. Rev. A 34, 4353 (1986)

[61] W.A. Tiller, K.A. Jackson, J.W. Rutter and B. Chalmers, Acta Metall. 1, 428 (1953)

[62] P. Haug, Nuclear Physics B, Proceedings Supplements 5A, 296 (1988)

[63] J.S. Langer, Rev. Mod. Phys. 52, 1 (1980)

[64] S.R. Coriell, G.B. McFadden and R.F. Sekerka, Ann. Rev. Mater. Sci. 15, 119 (1985)

[65] D.J. Wollkind, D.B. Oulton and R. Sriranganathan, J. Phys. (Paris) 45, 505 (1984)

[66] P.G. Drazin and W.H. Reid, Hydrodynamics Stability (Cambrige University Press, Cambrige) 1981

[67] W.A. Tiller, The Art and Science of Growing Crystals, J.J. Gilman ed. (J. Wiley & Sons. New York) 1966.

[68] C.D. Graham, Met. Progr. 71, 75 (1957)

[69] A. Aitta, G. Ahlers and D.S. Cannell, Phys. Rev. Lett. 54, 673 (1985)

[70] K.A Jackson and J.D. Hunt, Acta Met. 13, 1212 (1965)

[71] J.D. Hunt, K.A. Jackson and K.A. Brown, Rev. Sci. Instrum. 37, 805 (1966)

[72] Vitro Dynamics, Inc. (201) 625 1707

[73] Micro Mo Electronics Inc., (813)822 2529

[74] Velmex, Inc., (716) 624 1080

[75] Micro Kinetics Corp., (714) 476-9911

---

[76] Purchased from Newport Corporation, (800) 222 6440.

[77] *k*, determined by flurescence measurements in our lab.

[78] L.Williams, M. Muschol, X, Qian, W. Losert, and H.Z. Cummins, Physical Review E, Vol. 48, No. 1, 489, July 1993.

[79] C.A. Wulff and E.F. Westrum, J. Phys. Chem. 67, 2376 (1963)

[80] Bob Schaefer (Consortium on Casting of Aerospace of Alloys, NIST), Private communications.

[81] Bob Schaefer and M. Glicksman, Philosophical Magzine 32, 725 (1975)

[82] P. Coullet, L. Gil and D. Repaux, Phys. Rev. Lett. 62, 2957 (1989)

[83] L.H. Ungar and R.A. Brown, Phys. Rev. B 30, 3993 (1984).

[84] M. Muschol, D. Liu and H.Z. Cummins, Phys. Rev. A 46, 1038(1992)

[85] M.A. Eshelman and R.Trivedi, Acta Metall. 35, 2443 (1987)

[86] S.de Cheveigne, C. Guthmann, and M.M. Lebrun, J. Cryt. Growth 73, 242(1985)

[87] S. de Cheveigne, C. Guthmann, and M.M. Lebrun, J. Phys.(Paris) 47, 2095 (1986)

[88] J. Bechhoefer, P. Oswald, A. Libchaber, and C. Germain, Phys. Rev. A 37, 1691 (1988)

---

[89] John Bechhoefer, PhD thesis, University of Chicago (1988)

[90] S. de Cheveigne, C. Guthmann, P. Kurowski, E. Vicente, and H. Biloni, J. Cryt. Growth 92, 616 (1988)

[91] C. Misbah, J. Phys. (Paris) 50, 971 (1989)

[92] A. Karma, Phys. Rev. Lett. 57, 858 (1986)